CDDpress

www.nature.com/cddis

ARTICLE OPEN

Matrix Gla Protein drives stemness and tumor initiation in ovarian cancer

V. Nieddu[1], V. Melocchi[2], C. Battistini[1], G. Franciosa[3], M. Lupia[1], C. Stellato[1], G. Bertalot[4,5], J. V. Olsen[3], N. Colombo[6,7], F. Bianchi[2] and U. Cavallaro[1]✉

Ovarian cancer (OC) displays the highest mortality among gynecological tumors, mainly due to early peritoneal dissemination, the high frequency of tumor relapse following primary debulking, and the development of chemoresistance. All these events are thought to be initiated and sustained by a subpopulation of neoplastic cells, termed ovarian cancer stem cells (OCSC), that are endowed with self-renewing and tumor-initiating properties. This implies that interfering with OCSC function should offer novel therapeutic perspectives to defeat OC progression. To this aim, a better understanding of the molecular and functional makeup of OCSC in clinically relevant model systems is essential. We have profiled the transcriptome of OCSC vs. their bulk cell counterpart from a panel of patient-derived OC cell cultures. This revealed that Matrix Gla Protein (MGP), classically known as a calcification-preventing factor in cartilage and blood vessels, is markedly enriched in OCSC. Functional assays showed that MGP confers several stemness-associated traits to OC cells, including a transcriptional reprogramming. Patient-derived organotypic cultures pointed to the peritoneal microenvironment as a major inducer of MGP expression in OC cells. Furthermore, MGP was found to be necessary and sufficient for tumor initiation in OC mouse models, by shortening tumor latency and increasing dramatically the frequency of tumor-initiating cells. Mechanistically, MGP-driven OC stemness was mediated by the stimulation of Hedgehog signaling, in particular through the induction of the Hedgehog effector GLI1, thus highlighting a novel MGP/Hedgehog pathway axis in OCSC. Finally, MGP expression was found to correlate with poor prognosis in OC patients, and was increased in tumor tissue after chemotherapy, supporting the clinical relevance of our findings. Thus, MGP is a novel driver in OCSC pathophysiology, with a major role in stemness and in tumor initiation.

Cell Death and Disease (2023)14:220 ; https://doi.org/10.1038/s41419-023-05760-w

INTRODUCTION

Ovarian cancer (OC) is the deadliest gynecological tumor, with 313,959 new cases and 207,252 deaths worldwide in 2020 [1]. High-grade serous OC (HGSOC) is the most frequent type of OC (70%) with a survival rate of only 30% at 5 years [2]. Due to the lack of specific symptoms and screening methods, OC is frequently diagnosed at an advanced stage, when the tumor has already disseminated into the peritoneum. The standard of care for HGSOC is surgical cytoreduction followed by platinum-based chemotherapy. However, 70% of HGSOC relapse within 2 years [1], and almost all recurrent HGSOCs ultimately develop chemoresistance and become unresponsive to standard treatments [3]. Hence, new strategies to prevent, delay or treat tumor relapse in HGSOC patients remain an unmet need.

The clinical evolution of the disease seems to be accounted for by a small population of cells, called ovarian cancer stem cells (OCSC) [3]. Their stem-like features enable OCSC to initiate metastasis, drive tumor recurrence, and recapitulate the heterogeneity of the original tumor [4]. Furthermore, OCSC are able to elude the cytotoxicity of chemotherapeutics entering a quiescent state, increasing molecular pumps to efflux drugs outside the cells, and enhancing DNA repair and DNA damage response [5]. Hence, OCSC have emerged as optimal targets for novel OC-eradicating treatments. However, a detailed characterization of the molecular and functional traits of OCSC is still missing, partly due to the lack of clinically relevant experimental models. In fact, earlier studies on OCSC have mostly relied on cell lines that hardly recapitulate the biomolecular and histopathological features of HGSOC [3].

Our data identified Matrix Gla Protein (MGP) as one of the most prominent OCSC-associated genes. MGP encodes an extracellular matrix protein that belongs to the vitamin K-dependent protein family. It is secreted by chondrocytes and vascular smooth muscle cells and is expressed in vessels, cartilage, bone, lung, heart, and kidney [6]. MGP is classically known as a calcium chelator, mainly associated with the inhibition of tissue calcification in skeleton, coronary artery, and kidney [7]. MGP has also been found aberrantly expressed in different cancer types [8], including OC [9], where its level of expression often correlates with tumor

[1]Unit of Gynaecological Oncology Research, European Institute of Oncology IRCSS, Milan, Italy. [2]Cancer Biomarkers Unit, Fondazione IRCCS Casa Sollievo della Sofferenza, San Giovanni Rotondo, Foggia, Italy. [3]Proteomics Program, Novo Nordisk Foundation Center for Protein Research, University of Copenhagen, Copenhagen, Denmark. [4]Unità Operativa Multizonale di Anatomia Patologica, APSS, Trento, Italy. [5]Centre for Medical Sciences – CISMed, University of Trento, Trento, Italy. [6]Division of Gynecologic Oncology, European Institute of Oncology IRCSS, Milan, Italy. [7]University of Milan-Bicocca, Milan, Italy. ✉email: ugo.cavallaro@ieo.it

Edited by Gennaro Ciliberto

Received: 18 January 2023 Revised: 18 March 2023 Accepted: 20 March 2023
Published online: 28 March 2023

aggressiveness [10–12]. A few studies have also proposed a causal relationship between MGP expression and malignancy [13–15]. Yet, the biological mechanisms that regulate the functional contribution of MGP to cancer progression remain elusive. In particular, no information is available on the role of MGP in cancer stem cells (CSC), and also its involvement in OC development has not been investigated. Here, we report the novel role of MGP as a pivotal player in OCSC pathophysiology and as an effector of microenvironment-regulated OC stemness.

MATERIALS AND METHODS

Cell culture

Human ovarian carcinoma cell lines OVCAR3 were purchased from American Type Culture Collection (ATCC; cat# HTB-161), COV318 were acquired from Sigma (cat# 07071903). OVCAR3 cells were grown in RPMI 1640 medium (Euroclone, cat# ECM2001L) containing 20% fetal bovine serum (FBS, cat# RM10432), 2 mM L-glutamine (Lonza, cat# 17-605E), 100 U/ml penicillin, 100 µg/ml streptomycin (Euroclone, cat# LODE17602E), 10 µg/ml bovine insulin (Merck, cat# 91077 C). COV318 cells were cultured in DMEM (Euroclone, cat# ECM0103L) supplemented with 10% FBS, 100 µg/ml streptomycin, and 100 U/mL penicillin. The immortalized human mesothelial cell line MeT5A was kindly provided by Prof. Aldieri (Turin) and maintained in Medium 199 (Sigma, cat# M4530) containing 10% FBS, 3.3 nM epidermal growth factor (Merck, cat# E4127), 400 nM hydrocortisone (Sigma, cat# H0888), 870 nM Bovine insulin and 20 mM HEPES (Sigma, cat# H0887). Cell lines were routinely tested for mycoplasma with a PCR-based method and authenticated via short tandem repeat profiling.

Primary cell cultures were established from peritoneal ascites of high-grade serous ovarian cancer (HGSOC) patients. Samples were provided by the Division of Gynecology at the European Institute of Oncology (Milan) upon informed consent from patients undergoing surgery. Tumor histology was confirmed by a board-certified pathologist (GB), while the identity of cancer cells was confirmed by immunostaining for cytokeratins 5, 7, and 8, or for pan-cytokeratins. The purity of primary cell culture was consistently over 95%. Tissue isolation and culture conditions of primary cells were performed as described previously [16].

Mesothelial and fibroblasts were isolated from healthy omental specimens. The omentum was washed several times with sterile PBS, centrifuged at 1500 rpm for 5 min, and cultured with RPMI 1640, 20% FBS, and 100 U/ml penicillin, 100 µg/ml streptomycin. To isolate fibroblasts, the tissue was minced with scissors and razor and incubated overnight on an orbital shaker with 100 U of hyaluronidase (Merck, cat# H3884) and 1,000 U of collagenase type III (Worthington Biochemical, cat# LS004183) in DMEM, 10% FBS at 37 °C. The tissue was then centrifuged at 1500 rpm for 5 min, washed two times with PBS, and plated with DMEM, 10% FBS, 1% glutamine, 100 U/ml penicillin, 100 µg/ml streptomycin, 1% NEAA (Lonza, cat# 13-114E), 1% MEM vitamins (Lonza, cat# 13607C). Mesothelial and fibroblast cells were used for the experiments at early passages (1–3).

All cell lines and primary samples were maintained at 37 °C in a humidified incubator with 5% CO_2.

Sphere formation assay

Sphere formation assays were performed as described [17]. Briefly, single cell suspension derived from ovarian cancer cell lines or primary samples, were seeded at low density under non-adherent conditions in poly-(2-hydroxyethyl methacrylate) coated dishes (Sigma, cat# P3932-25G) and allowed to form monoclonal spheres. For ovarian cancer cell lines, OCSC-enriched sphere were maintained in DMEM:F-12 (1:1) (Gibco, cat# 11320033), supplemented with 2% B27 (Thermo Fisher Scientific, cat# 17504044;), 2 mM L-glutamine, 100 U/ml penicillin, 100 µg/ml streptomycin, 20 ng/mL EGF (Merck, cat# E4127), and 10 ng/mL fibroblast growth factor-2 (FGF2; Peprotech, cat# AF-100-18B). Cells were cultured at a density of 1000 cells/ml. Spheres were then dissociated with StemPro™ Accutase™ (Thermo Fisher Scientific, cat# A1110501), according to the manufacturer's protocol, and re-plated under the same conditions to obtain second-generation spheres.

Primary OCSC cultures were seeded at 5000 cells/ml in MEBM™ (Lonza, cat# CC-3151) supplemented with 2 mM L-glutamine, 100 U/mL penicillin, 100 µg/mL streptomycin, 5 µg/mL insulin, 0.5 µg/mL hydrocortisone, 1 U/mL heparin (Voden, cat # 07980), 2% B27, 20 ng/mL EGF, and 20 ng/mL FGF2.

Sphere formation was assessed 5–10 days after seeding. The sphere-forming efficiency (SFE) was defined as the ratio between the number of spheres counted and the number of cells seeded.

Affymetrix analysis

The Affymetrix analysis was performed as described [17] on patient-matched adherent cells and second-generation spheres derived from the 7 patients described in Table S2. After RNA extraction, samples were grouped into two independent pools of 4 and 3 samples, respectively. Total RNA was isolated using the miRNeasy Micro kit (Qiagen, cat# 217084) according to manufacturer's protocol and quantified using a NanoDrop 2000 (Thermo Scientific). The Ovation® Pico WTA System V2 (Nugen, cat# 3302-60) was used to amplify 5 ng of total RNA according to manufacturer's protocol. Quality control of the RNA samples was performed using an Agilent Bioanalyzer 2100 (Agilent Technologies). Each pool was labeled and hybridized to Affymetrix® Human Gene 2.1 ST according to the manufacturer instructions (Affymetrix). Quality control and normalization of Affymetrix.CEL files using the Robust Multi-array Average (RMA) were performed by Expression Console software (Affymetrix; version: 1.4.1.46). Microarray data analysis was performed using the BRB-ArrayTools (Version 4.4.0). Gene expression data were log2 transformed and probesets (psets) whose variance was in the bottom 75th percentile were excluded, for a total of 13,404 psets retained in the analysis. Class comparison analysis to identify differentially regulated genes was performed using t-test with a random variance model. The number of psets significant at 0.001 level of the univariate test was 2689 for a total of 1134 unique genes.

RNA extraction, qRT-PCR, and sequencing

Total RNA was extracted from adherent cultures or from spheres using the RNeasy Mini Kit (QIAGEN, cat# 217004) according to the manufacturer's protocol and quantified using the 2100 Bioanalyzer (Agilent). RNA quality control was checked using an Agilent 2100 Bioanalyzer (Agilent, Santa Clara, CA, USA). Preparation and hybridization of cDNA samples were performed at the Cogentech Microarray Unit (Milan, Italy; www.cogentech.it).

Gene expression levels for MGP, EMT, and stem genes were analyzed and normalized against housekeeping human GAPDH and HPRT1. TaqMan assays for specific genes are listed in Table S5. Normalized expression changes were determined with the comparative threshold cycle ($2^{-\Delta\Delta CT}$) method.

TruSeq kit and Illumina HiSeq2000 were used for RNA sequencing following the manufacturer's instructions. The sequencing coverage and quality statistics for each sample are summarized in Table S6.

RNA-Seq analysis

Poly-A enriched strand-specific libraries were generated with the TruSeq mRNA V2 sample preparation kit (Illumina, cat# RS-122-2001), ribosomal RNA depleted strand-specific RNA libraries with the TruSeq Stranded Total RNA LT sample preparation kit with Ribo-Zero Gold (Illumina, cat# RS-122-2301 and #RS-122-2302), and transcriptome capture based libraries with the TruSeq RNA Access Library Prep Kit (Illumina, cat# RS-301-2001). Recommended amounts of starting material were as follows: 100 ng of input RNA for TruSeq, 100 ng for Ribo-Zero, and 10 ng of intact RNA or 20 ng of degraded RNA for RNA access. All protocols were performed following the manufacturer's instructions. Libraries were sequenced by Illumina HiSeq2000 resulting in paired 50nt reads. Fastq files were aligned to the hg38 genome assembly using STAR. STAR gene counts were normalized applying the median of ratios method implemented in DESeq2 R package. Briefly, the normalization process implies different steps: (i) for each gene, a pseudo-reference sample is created and is equal to the geometric mean across all samples; (ii) for every gene in a sample and for each sample, the ratios sample/ref are calculated; (iii) the median value of all ratios for a given sample is taken as the normalization factor (size factor) for that sample; (iv) for each gene in each sample the normalized count values is calculated dividing each raw count value by the sample's normalization factor. For each gene, in each experimental condition (spheres cells and adherent cells), log2 Fold Change (log2FC) was calculated as the log2 ratio of normalized reads in MGP-overexpressing cells/KO cells vs. control cells.

Heatmaps and clusters were generated by using Cluster 3.0 for Mac OS X (C Clustering Library 1.56) and Java TreeView version 1.1.6r4 (uncentered correlation and centroid linkage) using median centered log2FC data.

Volcano plot were generated using R and log2FC data. Pre-Ranked Gene Set Enrichment Analysis (https://www.gsea-msigdb.org/gsea/index.jsp) was performed using log2FC of COV318 spheres and adherent cells, 1000 random gene sets permutation, weighted class metric, and hallmark of cancer and C2 curated Molecular Signatures Database gene sets29,30 (MSigDB). EnrichR analysis was performed on upregulated genes on COV318-MGP cells which showed an opposite regulation compared to OVCAR3-MGP^{KO}. We followed the instruction on the webtool https://amp.pharm.mssm.edu/Enrichr.

Immunoblotting

Cells, both bulk and spheres, were lysed in lysis buffer (4% SDS, 16% glycerol, 40 mM Tris-HCl [pH 6.8]) for 15 min at 90 °C, centrifuged for 5 min at 14,000 *g* and the supernatant was collected.

To prepare cytoplasmic extracts, the cells were washed with cold PBS and incubated with a buffer (10 mM Hepes pH 7.9; 1 M KCl; 0.1 mM EDTA; 0.1 mM EGTA, 1:500 protease, and phosphatase inhibitors) for 20 min on ice in a shaker. The cells were then scraped and collected in an eppendorf tube. After centrifugation for 10 min at maximum speed, the supernatant containing the cytoplasmic fraction was collected. To prepare nuclear extracts, the pellet was washed 3 times with the same buffer and then incubated with the hypotonic buffer (20 mM Hepes pH 7,9; 400 mM NaCl; 0.1 mM EDTA; 0.1 mM EGTA, 50% Glycerol; 1:500 protease and phosphatase inhibitors) for 1 h in a shaker at 4 °C. Nuclei were collected by centrifugation for 5 min at maximum speed.

Protein concentration was determined using a Pierce BCA Protein Assay kit (Thermo Fisher Scientific, Inc, cat# 23227) according to the manufacturer's instructions. Equal amounts of protein extracts (20 µg) were resolved in acrylamide gel and transferred onto nitrocellulose membranes. The membranes were incubated overnight at 4 °C with the following primary antibodies: MGP (Abcam, cat# ab86233, 1:500), GLI1 (cell signaling, cat# 2643S, 1:1000), vinculin (Sigma-Aldrich, cat# V9131, 1:10,000), actin (Abcam, cat# ab853, 1:3000), GAPDH (Sigma, cat# ABS16, 1:2000), Lamin A/C (Santa Cruz, cat# sc-7292, 1:500), α-tubulin (Santa Cruz, cat# sc-32293, 1:1000). Membranes were incubated with IgG HRP-conjugated secondary antibody (Bio-Rad Laboratories, cat# 1706515, 1706516, dilution 1:3000) for 1 h at room temperature. The signal was detected by the Clarity Western ECL Substrate (Bio-Rad, cat# 1705062) as described in the manufacturers protocol and the images were acquired using ChemiDoc (Bio-Rad) and analyzed with the Fiji software.

Proteome analysis

Cells were lysed with boiling guanidine-hydrochloride lysis buffer (6 M Gnd-HCl, 100 mM Tris-HCl pH 8.5, 5 TCEP, 10 mM CAA). Lysates were heated at 95 °C for 10 min, while shaking, and sonicated (Vibra-Cell VCX130, Sonics, Newtown, CT) for 2 min, with pulses 1 seconds on, 1 second off. Protein concentrations were determined using the Bradford assay (Bio-Rad). Proteins were pre-digested with endoproteinase Lys-C (Wako) for 2 h at room temperature in an enzyme/protein ratio of 1:100. Thereafter, samples were diluted to 1 M guanidine-hydrochloride with 25 mM Tris buffer before overnight digestion with trypsin (Sigma-Aldrich) at 37 °C in an enzyme/protein ratio of 1:50. After overnight digestion, enzymatic activity was quenched by acidifying the lysates using trifluoroacetic acid (TFA) at a final concentration of 1% and ensuring the pH of the samples being around 2. 750 ng of digested peptides for single-shot proteome analysis were loaded on C18 Evotips (Evosep) for MS analysis. Two technical replicates per sample were prepared.

Samples were analyzed on the Evosep One system [18] coupled to an Orbitrap Exploris 480 [19]. Samples were separated on an in-house packed 15 cm analytical column (150 µm inner diameter), packed with 1.9 µm C18 beads, and column temperature was maintained at 60 °C using an integrated column oven (PRSO-V1, Sonation GmbH) on the 30 samples per day gradient. The mass spectrometer was operated in positive ion mode, with spray voltage at 2 kV, heated capillary temperature at 275 °C, and funnel RF frequency at 40. Peptide match was set to off, and isotope exclusion was on. We used data-independent acquisition (DIA), with full MS resolution set to 120,000 at m/z 200 and full MS AGC target set at 300%, with an injection time of 45 ms. Scan range was set to 350–1400 m/z. AGC target value for fragment scan was set at 1000%. 49 windows of 13.7 Da were used with an overlap of 1 Da. The MS/MS acquisition was set to 15,000 resolution, and injection time to 22 ms. Normalized collision energy was set at 27%.

DIA raw files were analyzed on Spectronaut [20] v 15.5.211111.50606 in directDIA mode with standard settings. Deamidation of asparagine and glutamine (NQ) was added as variable modification. Data filtering was set on "q value sparse" (default in version 15). The Human Uniprot fasta file (downloaded in October 2020; 20,600 entries) was supplemented with the MaxQuant contaminant fasta file containing 246 entries.

The plot shown in Fig. 1C was generated using the R software v4.1.1 (with RStudio v1.2.504) with the ggplot2 package v3.3.5.

Immunofluorescence

OVCAR3 and COV318 cells were seeded on coverslips and grown to a near-confluent state. Cells were fixed with 4% paraformaldehyde for 10 min at room temperature and then permeabilized in ice-cold PBS, 0.5% Triton X-100 for 3 min at 4 °C. After blocking for 1 h at room temperature in a humid chamber with blocking buffer (PBS, 2% BSA, 5% donkey serum, and 0.05% Triton X-100), the cells were incubated for 2 h with the anti-MGP primary antibody (Abcam, cat# ab86233, 1:50) diluted in blocking buffer. Coverslips were then washed with PBS and incubated with the secondary antibodies for 1 h at room temperature (Jackson Immuno Research Laboratories, Cy5 Donkey anti-rabbit, cat# 711-175-152, 1:400). Nuclei were then counterstained with 0.2 µg/ml DAPI (Sigma-Aldrich, cat# 32670-25MG-F) and the coverslips were mounted in Mowiol (Merck, cat# 81381). Images were acquired using the Leica MultiFluo microscope.

Cell viability

Ovarian cancer cells were seeded in 96-well plates (1.5*10^3 cells/well in quadruplicate) and incubated for 24-48-72-96 h. After each time point, the metabolic activity was quantified using the Cell counting kit-8 (Sigma-Aldrich, cat# 96992), following the manufacturer's instructions. The absorbance at a wavelength of 450 nm was measured using the Glomax Plate Reader.

Adhesion assay

MeT5A-RFP were seeded at 2*10^4 cells/well into a 96-well plate and incubated for 24 h at 37 °C in order to obtain a cell monolayer. 7*10^3 single cells derived from second-generation spheres were labeled with 1 mM CMFDA (Life Technologies, cat# C7025) for 30 min and added on top of the mesothelial monolayer. The cells were washed after 8 h. The attached cells were imaged using a Nikon Eclipse microscope and counted using the Image J software.

Mesothelial clearance assay

MeT5A-RFP were plated into a 96-well plate at 2*10^4 cells/well and incubated for 24 h at 37 °C in order to obtain a cell monolayer. Ovarian cancer spheroids were formed by incubating 3*10^2 cells/well in a poly-HEMA coated 96-well round-bottom plate at 37 °C for 24 h. The spheroids were then transferred onto the mesothelial monolayer and the co-cultures were imaged every 2 h for 72 h using a Nikon Eclipse microscope.

The invasive area created by the aggregates in the mesothelial monolayer was measured and the clearance was calculated normalizing the cell-free area created by the spheroid with the aggregate size at time 0. Representative images were selected and combined in Image J software to get the clearance videos.

3D organotypic model

The 3D organotypic model was assembled by plating in each well of a 6-well plate 6*10^4 primary omental fibroblasts mixed with 7.5 µg of collagen-I and 7.5 µg of fibronectin at 37 °C. After 4 h, 3*10^5 primary mesothelial cells were added to the culture and incubated at 37 C for 2 days. Single-cell suspensions of primary HGSOC cells, pre-labeled with 1 µM CMFDA for 15 min, were seeded on top of 3D organotypic cultures. After 48 h, the co-cultures were dissociated to single cells and CMFDA-labeled HGSOC cells were isolated by FACS sorting and subjected to RNA extraction.

When the 3D organotypic model was established using cell lines, IMR90 (fibroblasts), MeT5A (mesothelial) and OVCAR3 (either control or MGP^{KO}) were employed, and after FACS sorting tumor cells were subjected both to RNA extraction and to sphere formation assays.

Cell treatments with Hedgehog inhibitors

Second-generation spheres from COV318-CTR or COV318-MGP cells were seeded at 1*10^3 cells/ml in triplicate in polyHEMA-coated 6-well plates. Sphere culture and SFE measurement were performed as described above.

The following Hedgehog inhibitors were used in sphere formation assays at the concentrations indicated in the figures: GANT61 (Selleckem, cat# S8075), Cyclopamine (Fisher scientific, cat# J61528.MB), and Vismodegib (Selleckem, cat# S1082). SFE was determined 7 days after treatment.

Immunohistochemistry

Immunohistochemical (IHC) staining from human tissue microarray or mouse xenograft samples was performed on 3-µm-thick sections from formalin-fixed paraffin-embedded samples and dried in a 37 °C oven overnight. Hematoxylin/eosin (H&E) staining was performed with H&E Leica Kit Infinity for a full automated autostainer (Leica ST5020). IHC staining for Ki67 and MGP antibodies was performed using Bond III IHC autostainer for full Automated Immunohistochemistry (Leica biosystems). Antigen was unmasked with Tris-EDTA pH 9 (Bond Epitop Retrival Solution 2 Leica, cat# AR9640). Both mouse monoclonal anti-Ki67 CloneMIB-1 (Dako, cat# M7240) and rabbit polyclonal antibody MGP (ProteinTech, cat# 10734-1-AP) were used at 1:200. The antibodies were diluted with Bond Primary Antibody Diluent AR9352 Leica. BOND IHC Polymer Detection Kit (cat# DS9800) was used to stain both antibody with DAB Cromogen. IHC samples were counterstained using Hematoxylin solution (Leica, cat# RE7107-CE). Pictures of stained sections were acquired with the Aperio ScanScope XT instrument. Ki67 and MGP staining were analyzed and scored by a board-certified pathologist (GB).

Lentivirus production and cell transduction

For lentiviral infection, HEK293T was used as the packaging cell line. HEK293T were co-transfected, using the calcium phosphate precipitation method, with 10 µg of lentiviral vectors either empty vector (EX-NEG-Lv122; GeneCopoeia) or containing the cDNA for human MGP (EX-Z9471-Lv122; GeneCopoeia), and the following packaging vectors: PMD2G, RRE, and REV.

The supernatant from HEK293T containing the virus particles was supplemented with 8 µg/mL of polybrene and used to infect COV318 cells, generating the COV318-CTR and COV318-MGP cell lines upon selection with 2.5 µg/ml puromycin. Overexpression of MGP was confirmed by Western blot analysis and immunofluorescence.

CRISPR-Cas9

Single guide RNA (sgRNA) sequences to target MGP gene in the exon 1 region were designed using the online web tool for CRISPR (https://chopchop.cbu.uib.no [21];). Two sgRNA were selected (GCCTTCCACTAA-CATCCCGTAGG and CAAAGTTACTACCGCTAAGGCGG) in order to perform a dual guide targeting approach. Both guide sequences were then cloned as DNA inserts into pSpCas9 (BB)-2A-GFP (pX458) (Addgene plasmid, cat# 48138; a gift from Bruno Amati, Milan, Italy), encoding also the Cas9 protein and GFP.

To generate stable OVCAR3 knock-out cell lines, 10 µg pX458 encoding Cas9 and sgRNAs were transfected using Lipofectamine 3000 (Thermo-Fisher, cat# L3000008), according to manufacturer's instruction. Sorting of GFP-positive cells was performed 48 h after transfection and $1*10^3$ cells were plated onto a 15-cm dish. Clones were isolated 10–15 days later and MGP-knockout clones were identified by PCR and Sanger sequencing.

In vivo models

6–8 week-old NOD/SCID IL2R-gamma null (NSG) female mice (from Charles River Laboratories) were injected subcutaneously into the flank with ovarian cancer cells in a 1:1 (vol:vol) mixture with growth factor-reduced Matrigel (Corning, cat# 356231) and phosphate-buffered saline (PBS), with a final volume of 100 µl per injection. Each experimental group consists of 6 mice for COV318 or 10 mice for OVCAR3.

For limiting dilution experiments, mice were injected with serial dilutions of COV318-CTR or COV318-MGP cells ranging between $1*10^6$ and 10 cells/site, while $5*10^6$ OVCAR3-CTR or OVCAR3-MGP^{KO} cells/site were injected into the mice flank.

Tumor latency was defined as the time interval from the injection to the formation of palpable tumors. Tumor take was determined as number of mice with palpable tumors. Tumor size was monitored by caliper measurement and the growth curves of different tumors were calculated with the formula: Tumor Volume = 1/2*(length × $width^2$).

Body weight and general physical status were monitored daily, and the mice were sacrificed when the tumor reached 1.2 cm in diameter. Survival curves were drawn using the Kaplan-Meier method. The log-rank Mantel-Cox test was employed to define any statistical difference between the survival curves of the groups. The stem cells frequency was measured using the ELDA online Software http://bioinf.wehi.edu.au/software/elda.

All mice were age-matched and then randomized into the different groups. All experimental procedures involving mice and their care were conducted in conformity to the following laws, regulations, and policies governing the care and use of laboratory animals: Italian Law (D.lgs 26/2014, authorization no. 19/2008-A issued 6 March 2008 by the Ministry of Health); internal protocol approved by the fully authorized animal facility of European Institute of Oncology and by the Italian Ministry of Health (IACUC no. 25/2015). Mice were housed under specific pathogen-free conditions in isolated vented cages and allowed access to food and water ad libitum.

TCGA-HGSOC data analysis

Total RNA-seq gene expression data ($N = 307$) and clinical data for TCGA patients with high-grade serous ovarian adenocarcinoma (TCGA-HGSOC) available at cBIOportal (https://www.cbioportal.org/) were used. For single-sample gene set enrichment analysis (ssGSEA) of RNA-seq TCGA cohort, enrichment scores were calculated by using the GSVA package in [22] and gene sets of Molecular Signatures Database (MSigDB) [23, 24] related to stemness (STEM), epithelial-to-mesenchymal transition (EMT) and hallmarks of cancer. Spearman correlation coefficients between ssGSEA results and MGP expression, and *p*-values were calculated using R (R Core Team (2021). R: A language and environment for statistical computing. R Foundation for Statistical Computing, Vienna, Austria. URL https://www.R-project.org/). For survival analyses we downloaded MGP copy number variants classification (CNV, $N = 579$) and MGP microarray gene expression data z-score classification (z-score cut-off for high expression = +1.5, $N = 538$) for TCGA patients with high-grade serous ovarian adenocarcinoma (TCGA-HGSOC) available at cBIOportal (https://www.cbioportal.org/). Overall survival (OS) and disease-free survival (DFS) were estimated by the Kaplan-Meier method. Follow-up was truncated at 5 years in order to reduce the potential overestimation of overall mortality with respect to ovarian-cancer-specific mortality. All survival analyses were performed using the JMP software, version 16 (SAS Institute Inc., Cary, NC, 1989–2021).

Statistical analysis

Independent experiments were considered as biological replicates. When performed, technical replicates deriving from the same biological replicate were averaged. For in vivo experiments, each mouse represented one biological replicate. If not indicated otherwise, data are expressed as means ± SEM, calculated from at least three independent experiments. Student's two-tailed t-test was used to compare SFE values among the groups while one-way ANOVA multiple comparison test was employed to compare two or three groups and to determine statistical significance (GraphPad Prism 8). Cut-off threshold to define significance was set at $p < 0.05$. Asterisks correspond to *p*-value calculated by two-tailed, unpaired, t-test (*$p < 0.05$, **$p < 0.01$, ***$p < 0.001$, ****$p < 0.0001$). The sample size estimation was based on previous studies and pilot experiments.

RESULTS

MGP is upregulated in patient-derived OCSC

Primary cell cultures were established from tumor samples derived from HGSOC patients. The formation of single cell-derived spheroids under non-adherent conditions was employed in order to enrich for OCSC [17]. Patient-matched bulk, adherent tumor cells and OCSC-enriched spheroids were subjected to Affymetrix analysis and the transcriptomes were compared. A total of 2689 transcripts corresponding to 1176 genes ($p < 0.001$, two-sample t-test with random variance model) were found to be differentially regulated between bulk and OCSC, with 560 genes upregulated and 616 genes downregulated in OCSC (Table S1). In agreement with previous observations [17], a subset of classical stemness-related genes were differentially expressed in spheroids vs. bulk tumor cells (Suppl. Fig. S1). Among the upregulated genes we found MGP (FC = 5.0, FDR = 0.002; Fig. 1A), a gene that encodes for Matrix Gla Protein (MGP). Since MGP has never been associated with OCSC and very little is known about its function in cancer, we decided to investigate whether it plays any role in OCSC

pathophysiology. First, we confirmed by RT-qPCR, in six patient-derived samples, the upregulation of MGP in OCSC as compared to their bulk counterpart (Fig. 1B). The data were also validated at the protein level, both by mass spectrometry-based proteomics in ten patient-derived samples (Fig. 1C and Suppl. Fig. S2A) and by western blotting in three patient-derived samples (Fig. 1D). Thus, MGP is consistently enriched in patient-derived OCSC. We also attempted to test whether MGP expression correlates with stemness-associated genes in HGSOC transcriptome datasets. To this goal, we performed a single-sample gene set enrichment analysis (ssGSEA) from 370 HGSOC patients included in the TCGA cohort. Overall, a positive and significant correlation could be found between MGP and gene sets related to stemness (Fig. 1E). Furthermore, the correlation extended also to gene sets related to epithelial-mesenchymal transition (EMT), which is a common feature of cancer stem cells [25]. In this regard, it is noteworthy that also in the context of the hallmarks' gene sets MGP expression correlated with EMT (Fig. 1F).

MGP is necessary and sufficient for OCSC features

To identify experimental models suitable to explore the functional role of MGP in OCSC, the protein level of MGP was evaluated in a panel of OC cell lines that have been classified as HGSOC-like models [26, 27]. We found that COV318, COV362, and Kuramochi cells expressed no or very low amounts of MGP, whereas the protein was readily detectable in Tyk-nu, OVCAR3, and OV90 cells (Suppl. Fig. S2B). Thus, COV318 and OVCAR3 were selected for the genetic manipulation of MGP in gain- and loss-of-function experiments, respectively. Endogenous MGP expression in OVCAR3 was ablated through the CRISPR-Cas9 technology and validated by RT-qPCR, western blot, and immunofluorescence (Suppl. Fig. S2C–E). The ectopic expression of MGP in COV318 was achieved via lentiviral transduction, followed by validation (Suppl. Fig. S2F–H). Notably, neither knockout nor overexpression of MGP showed any effect on cell proliferation in standard 2D cultures (Suppl. Fig. S2I).

To investigate the contribution of MGP to OC stem-like features, we first took advantage of the sphere formation assay, which reflects the ability of CSC to resist to anoikis, to self-renew, and to proliferate when cultured at low density under non-adherent conditions, generating monoclonal sphere-like structures [28]. The ablation of MGP expression significantly reduced the sphere-forming ability of OVCAR3, while MGP overexpression enhanced the spherogenicity of COV318 (Fig. 2A and Suppl. Fig. S3A). This demonstrated that MGP is causally involved in sphere formation and implicated for the first time MGP in OC stemness.

EGF and FGF2 are required for sphere formation in various stem cell models [17, 29, 30]. Surprisingly, we discovered that COV318-MGP cells, but not COV318-CTR, were able to generate spheres in the absence of growth factors (Fig. 2B), indicating that MGP is able to enhance OCSC function even under stringent conditions.

As a first attempt to elucidate the molecular mechanisms that underlie the role of MGP in the stem-like traits of OC cells, we tested whether MGP regulates the expression of genes involved in key aspects of stemness, namely multipotency and epithelial-mesenchymal transition (EMT). Indeed, the knock-out of MGP decreased the expression of several multipotency-associated genes, such as *KLF4*, *NANOG*, *POU5F1*, and *SOX2*, while the ectopic expression of MGP induced their upregulation (Fig. 2C). A similar MGP-dependent regulation was observed for a subset of EMT-associated genes, including *CDH2*, *SNAI2*, *FN1* and *ZEB1* (Fig. 2C).

Taken together, these results support the notion that MGP confers stem-like traits to OC cells.

MGP promotes OC cell adhesion and invasion of the mesothelium

Adhesion to and invasion of mesothelium are key steps in the peritoneal dissemination of OC, and OCSC are thought to play a pivotal role in this context, due to their ability to self-renew and to initiate the formation of metastatic and/or recurrent tumors [3]. Therefore, we evaluated whether MGP influences the adhesiveness of OCSC to the mesothelium. OCSC derived from second-generation spheres of OVCAR3 or COV318, with MGP knockout or ectopic expression, respectively, were seeded on top of a mesothelial layer formed by MeT5A cells, and the number of attached cells was measured after 8 h. OVCAR3-MGP^{KO} cells exhibited a reduced adhesion ability compared to OVCAR3-CTR cells, while COV318-MGP showed significantly higher adhesion respect to COV318-mock (Fig. 3A). These data causally implicate MGP in the mesothelial adhesion of OCSC.

To evaluate the functional role of MGP in mesothelial invasion, we employed the mesothelial clearance assay that recapitulates the early steps of OC peritoneal colonization [31]. Cell aggregates derived from OVCAR3-MGP^{KO} or COV318-MGP cells (or their respective controls) were plated on the mesothelial monolayer and their ability to breach and invade the monolayer itself was monitored over three days. As shown in Fig. 3B and in Suppl. videos 1 and 2, MGP ablation resulted in a decreased invasion of OVCAR3 cells, while the ectopic expression of MGP in COV318 cells enhanced their mesothelial invasion capability (Fig. 3C). The quantitation in Fig. 3B, C (right panels) shows that MGP exerted quite a dramatic effect on the mesothelial clearance potential of OC cells.

MGP is upregulated by the TME and is required for TME-enhanced sphere formation

In an attempt to elucidate the biological basis of MGP enrichment in OCSC, we built on the notion that the tumor microenvironment (TME) influences several aspects of OC stemness [32] and, therefore, could be involved in the regulation of MGP expression in OCSC. We first tested this hypothesis in a clinically relevant setting consisting of an in vitro 3D organotypic model, derived from the patient's omentum, that recapitulates the peritoneal TME [33]. Patient-derived primary OC cells were co-cultured with the 3D TME (Fig. 4A) followed by the RT-qPCR assay for the expression of MGP. In primary cultures from four independent patients, a remarkable upregulation of MGP was observed in cancer cells co-cultured with the TME as compared with cells that had no contact with the TME (Fig. 4B). Analogous effects were observed on a panel of OC-derived cell lines, including OVCAR3 and COV318 (Suppl. Fig. S3B). The peritoneal TME-dependent induction of MGP expression in OC cells implicates the TME in the regulation of cancer stemness. Along this line, the co-culture with the TME did indeed enhance the sphere-forming ability of OVCAR3 cells (Fig. 4C). Of note, MGP ablation abrogated sphere formation both in the absence and in the presence of TME (Figs. 2A, C), which implicates the molecule in both TME-induced and cell-autonomous spherogenesis.

MGP is involved in OCSC-driven tumorigenesis

Since tumor initiation is a defining feature of CSC, we asked whether MGP modulates the tumor-initiating potential of OC cells. NOD/SCID/IL2Rgamma-null mice were inoculated subcutaneously with OVCAR3 or COV318 genetically manipulated for MGP expression and monitored for tumor development.

We first determined the rate of tumor take in OVCAR3-CTR vs. OVCAR3-MGP^{KO} cells (5*10^6 cells/mouse). As shown in Fig. 5A, a dramatic reduction in tumor initiation was observed upon ablation of MGP: at 100 days post-injection, 10 out of 10 mice with OVCAR3-CTR cells developed tumors, while no tumors were observed in the MGP-knockout group. Furthermore, at day 200 only 2 mice out of 10 injected with OVCAR3-MGP^{KO} cells developed tumors.

We observed a dramatic difference also in tumor growth, with control tumors reaching an exponential growth phase starting on day 60, whereas the tumors in the two mice with OVCAR3-MGP^{KO} cells

failed to develop beyond a barely palpable size (Fig. 5B). Accordingly, all mice with OVCAR3-MGP^{KO} cells were all alive after 360 days, in contrast with the short survival of OVCAR3-CTR mice (Fig. 5C). Thus, MGP was required for both tumor initiation and growth.

These results raised the hypothesis that MGP increases the frequency of tumor-initiating cells in a population of OC cells. To test such a possibility, we performed in vivo extreme limiting dilution assays (ELDA); Ref. [34] with COV318 cells expressing MGP

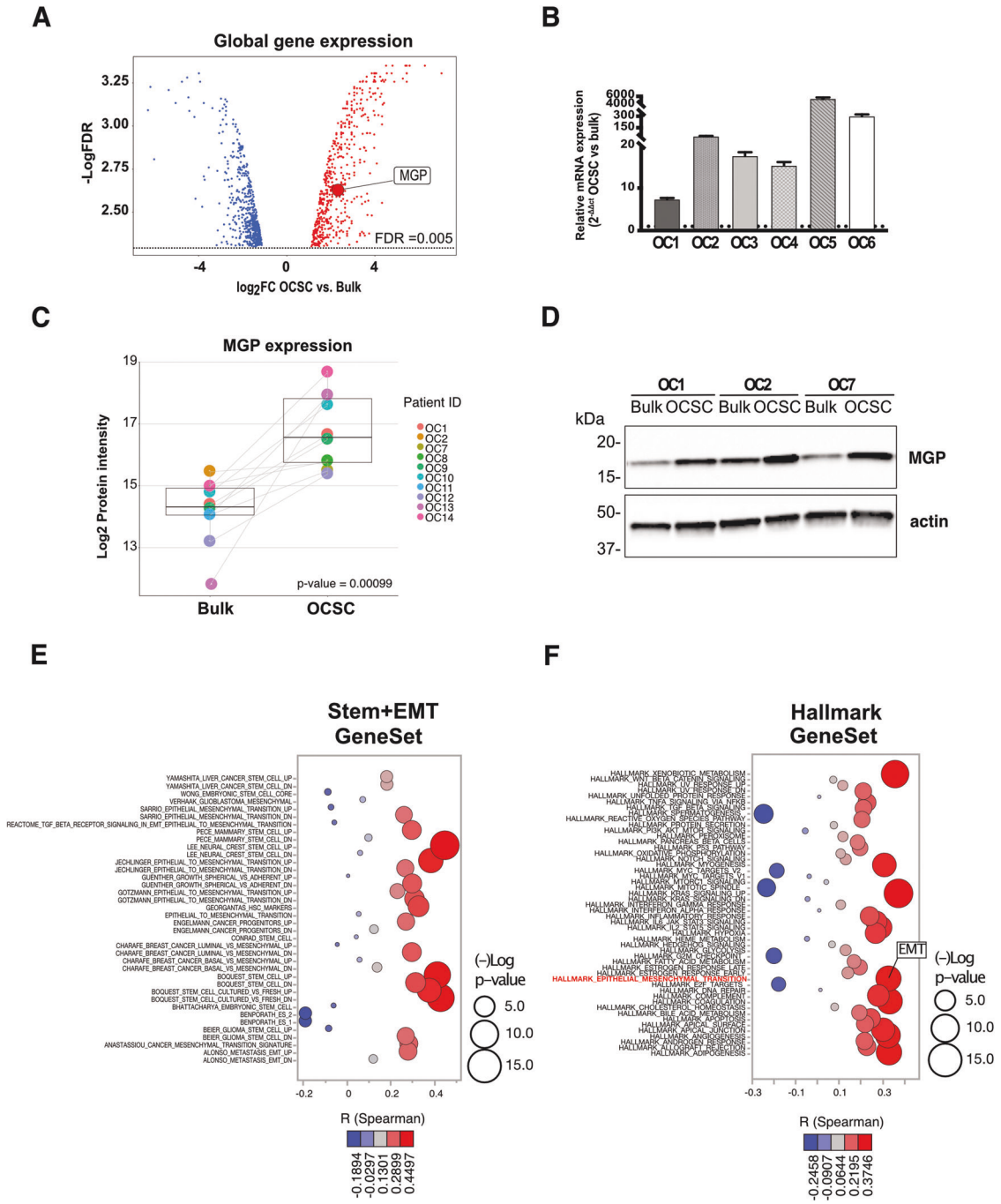

Fig. 1 Upregulation of MGP in patient-derived OCSC. A Volcano plot showing the significantly differentially expressed genes (False Discovery Rate (FDR) ≤ 0.005) between primary spheres (OCSC) and adherent (bulk) cells from seven patients. The x-axis represents the log2 fold change (log2FC; OCSC vs. bulk cells). DEGs with log2FC ≥ 1 and log2FC ≤ −1 are shown in red and blue, respectively. The y-axis represents the -Log False Discovery Rate (-Log FDR). MGP is indicated among the genes upregulated in OCSC. **B** MGP mRNA expression was analyzed by qRT-PCR. Data are represented as a relative mRNA expression ($2^{-\Delta\Delta Ct}$) of MGP cultured as spheres as compared to their bulk counterpart (dashed line). **C** Normalized protein intensity for the protein MGP in ten patient-derived pairs of primary bulk OC cells and OCSC. The *p*-value was calculated by two-sided paired two-sample t-test. **D** Primary ovarian cancer cells from three independent patients (OC1, OC2 and OC7) were grown under bulk or OCSC conditions. Cell lysates were immunoblotted for MGP and actin was used as loading control. Bubble plots showing ssGSEA results using the STEM + EMT GeneSets (panel **E**; $N = 38$) or the HALLMARK GeneSets (panel **F**; $N = 50$). Y-axes, GeneSets; X-axes, Spearman correlation coefficient (R) between MGP expression and ssGSEA scores in the TCGA-HGSOC cohort. Bubble size is proportional to inverse of Logarithmic (-Log) of significance [e.g., -Log(*p*-value) =5, *p*-value <10^{-6}; student's *t*-test] of Spearman correlation coefficient (R). Bubble colours refer to Spearman correlation coefficients (R), as per the legend.

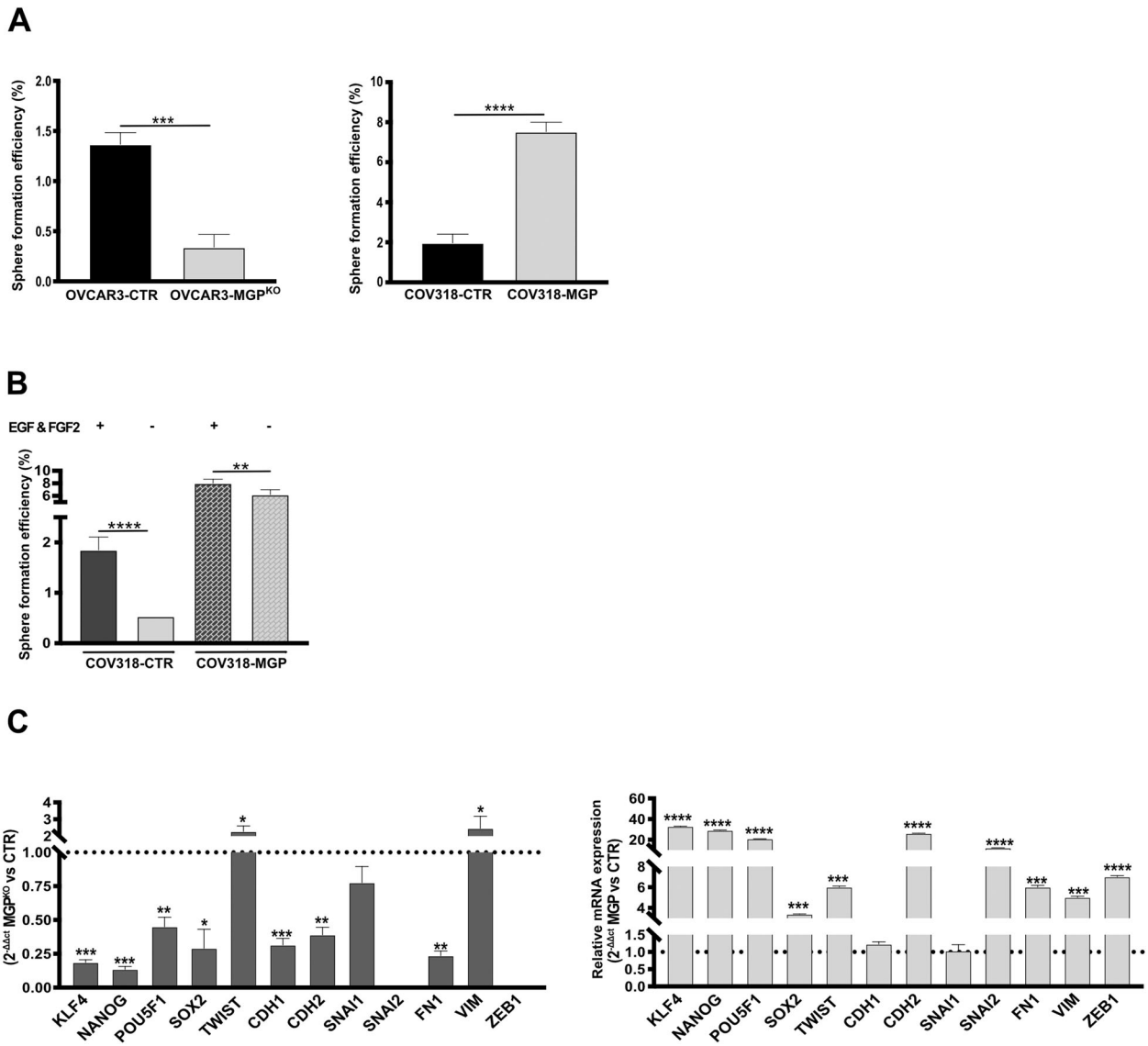

Fig. 2 MGP modulates stemness-related features. A Sphere formation assay on second-generation spheres performed on MGP-manipulated cell lines. The experiment was conducted in triplicate and data are expressed as means ± SD. ***$p < 0.001$, ****$p < 0.0001$. **B** Sphere formation assay carried out on COV318-CTR or COV318-MGP in medium depleted of both EGF and FGF2. **$p < 0.01$, ****$p < 0.0001$. **C** qRT-PCR for stemness and EMT-related genes on second-generation spheres from OVCAR3 (left) and COV318 (right). Data are expressed as relative mRNA level ($2^{-\Delta\Delta Ct}$) and normalized to the corresponding control cultures (dashed line). Data refer to means ± SD from a representative experiment performed in triplicate.

ectopically. Mice were injected with decreasing numbers of cells, ranging from $1*10^6$ to 10 cells/mouse, and then monitored for tumor formation. In agreement with the results on genetically manipulated OVCAR3 cells, MGP increased dramatically the tumor-initiating potential of COV318 cells. Indeed, tumor formation was observed at day 20 with as few as 500 cells in MGP-expressing cells, while $2*10^5$ cells were necessary to detect tumors with control COV318 cells at the same time point (Fig. 6A). ELDA calculations revealed that the frequency of tumor-initiating cells increased from 1/296,618 in COV318-CTR to 1/277 in COV318-MGP cells (1071 times; Fig. 6A), in line with MGP promoting a dramatic expansion of cells with tumorigenic capacity.

Besides tumor initiation, the ectopic expression of MGP also enhanced and sustained COV318 tumor growth. Among COV318-CTR mice, only the animals injected with $1*10^6$ and a fraction of those injected with $2*10^5$ or $2*10^4$ cells developed tumors, while lower cell numbers formed either no tumors or palpable lesions that remained small even after 10 months (Fig. 6B, left). On the contrary, in the COV318-MGP group all mice developed tumors, including those inoculated with 10 cells, and all tumors exhibited exponential growth (Fig. 6B, right). Accordingly, COV318-MGP tumors contained a remarkably higher frequency of proliferating, Ki67-positive cells as compared to control tumors (Suppl. Fig S3C). Along the same line, COV318-MGP tumors resulted in short survival even with low cancer cell numbers, while survival was markedly longer for COV318-CTR mice, with animals being still alive at 10 months when injected with up to $2*10^4$ cells (Fig. 6C).

These data indicated a major role for MGP in tumor initiation and development. Taken together, both gain and loss-of-function approaches pointed to MGP as a driver in OCSC pathophysiology and revealed that MGP is not only associated to the OCSC phenotype but is actually implicated in OCSC-driven malignancy.

MGP promotes OC stemness via GLI1

To elucidate the molecular mechanisms underlying the role of MGP in OCSC, and to identify downstream effectors, we first

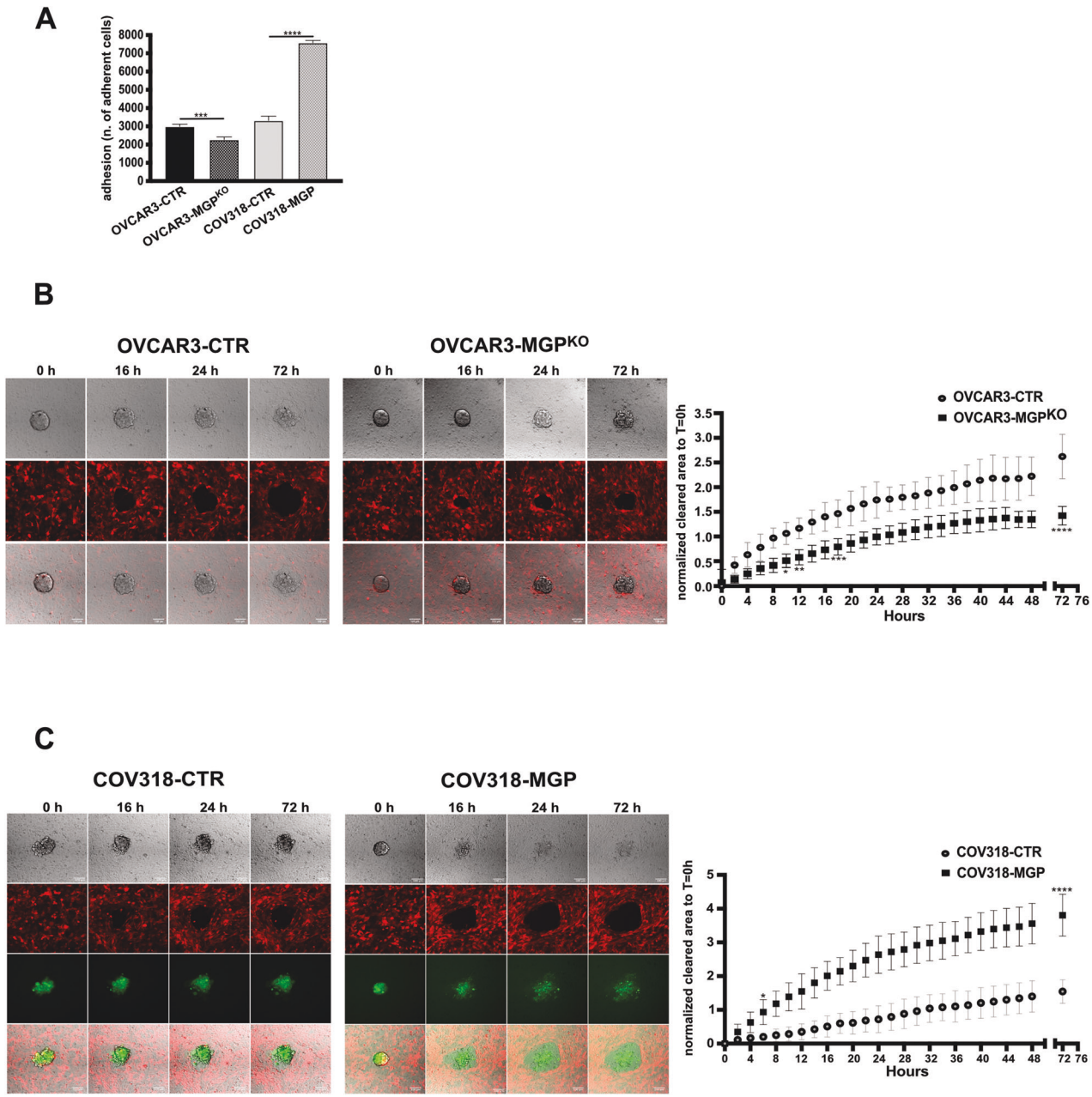

Fig. 3 MGP regulates mesothelial invasion of ovarian cancer cells. A Adhesion of OVCAR3 (control vs MGP-knockout) or COV318 (control vs MGP-overexpressing) onto a monolayer of MeT5A-RFP cells. Results are expressed as number of adherent cancer cells as counted 8 h after seeding. Data are expressed as means ± SD from two independent experiments each performed in sestuplicate. ***$p < 0.001$ and ****$p < 0.0001$. Mesothelial clearance assays of OVCAR3 CTR or MGP^{KO} (**B**) and COV318 CTR or MGP (**C**). Images were taken at the indicated time points. The graphs on the side show the quantification of the cleared areas calculated every 2 h (from 0 to 72 h). Data are shown as means ± SD from 26 aggregates for each condition obtained from 3 independent experiments. *$p < 0.05$, **$p < 0.01$, ***$p < 0.001$, ****$p < 0.0001$. Scale bar, 100 µm.

defined the impact of manipulating MGP expression on the transcriptome of these cells. RNA-seq analysis was carried out in MGP-manipulated vs. control cells, comparing bulk with OCSC. We found 1624 genes differentially regulated in bulk cells (Suppl. Fig. S3D and Table S3) and 999 in OCSC (Fig. 7A and Table S4) that showed opposite trend of regulation upon either MGP ablation in OVCAR3 cells or overexpression in COV318 cells, thus implicating MGP as a master modulator of OC transcriptome. We then applied a reverse engineering approach based on EnrichR to identify molecular mechanisms modulated by MGP. This revealed several tumor-associated pathways in both bulk (Suppl. Fig. S3E) and in OCSC (Fig. 7B), with the latter enriched in pathways classically implicated in stemness (*e.g.*, EMT, WNT/β-catenin, estrogen response). A subset of these pathways was also identified by a GSEA approach (Suppl. Fig. S3F).

One of the most prominent pathways modulated by MGP in OCSC was Hedgehog signaling (Fig. 7B and Suppl. Fig. S3F), a pathway that has been implicated in stem-like properties of OC cells [35] but for which a link with MGP has never been reported. A GSEA confirmed the MGP-induced activation of the Hedgehog pathway in OCSC (Fig. 7C). Accordingly, the transcription factor GLI1, a major effector of Hedgehog signaling, was among the top-ranking genes regulated by MGP in OCSC (Fig. 7D). The upregulation of GLI1 in MGP-overexpressing cells and its

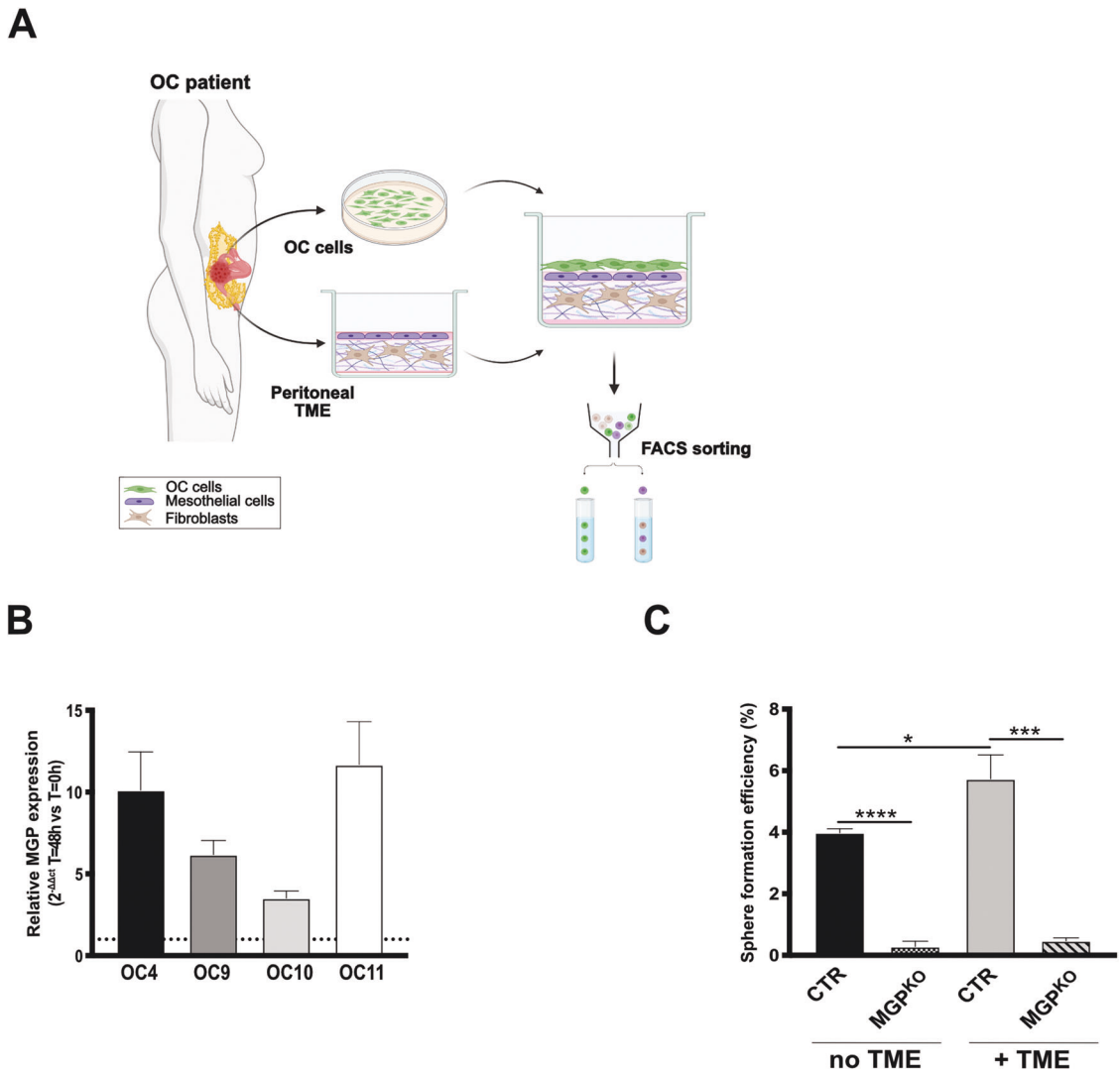

Fig. 4 MGP in ovarian cancer cells is upregulated by the tumor microenvironment. A Schematic representation of the workflow used for the co-cultured of OC cells with the tumor microenvironment. Created with BioRender.com. **B** qRT-PCR for MGP on primary ovarian cancer cells from four independent patients co-cultured with the TME for 48 h. Data are expressed as relative mRNA level ($2^{-\Delta\Delta Ct}$) and normalized to the corresponding cells not co-cultured with TME (dashed line). Data refer to means ± SD from a representative experiment performed in triplicate. **C** Sphere formation assay on OVCAR3-CTR and OVCAR3-MGP^{KO} after a 48-h co-culture with TME or without.

downregulation in MGP-knockdown cells was validated at both the mRNA and the protein levels (Fig. 7E, F). Since the activation of GLI1 upon Hedgehog pathway stimulation is a direct consequence of its nuclear translocation, we tested the intracellular localization of the protein through subcellular fractionation. As shown in Fig. 7G, the overexpression of MGP resulted in massive accumulation of GLI1 in the nucleus of COV318 cells, further supporting the connection between MGP and Hedgehog signaling. We then asked whether GLI1-mediated Hedgehog signaling is involved in the regulation of OC stemness by MGP. The activation of the Hedgehog pathway can occur in a canonical, Patched1/Smoothened-mediated manner (PTCH1-SMO-GLI1; Ref. [36]) or in a non-canonical way, which refers to the SMO-independent activation of GLI1 [37]. GANT61, a specific GLI1 inhibitor which targets both canonical and non-canonical Hedgehog pathway [38], reduced MGP-driven, but not basal, sphere formation in a dose-dependent manner (Fig. 8A). Analogous results were obtained with cyclopamine (Fig. 8B), which influences the balance between the active and inactive forms of Smoothened and inhibits specifically the canonical pathway [39]. Notably, the cyclopamine derivative vismodegib, an FDA-approved Hedgehog inhibitor [40], also reduced MGP-dependent sphere formation dose-dependently (Suppl. Fig. S3G). Thus, MGP-induced sphere formation in OC cells occurred through the canonical Hedgehog pathway. To further elucidate the role of Hedgehog signaling as an effector of the stem-like phenotype promoted by MGP, we tested whether GLI1 is involved in the induction of multipotency and EMT-related genes. As shown in Fig. 8C, GANT61 efficiently reduced the MGP-dependent upregulation of *KLF4, NANOG, POUF1* and *SOX2*, as well as of several genes associated with EMT (*TWIST1, CDH2, SNAI2, FN1, VIM, ZEB1*). On the contrary, the same genes were not affected by the GLI1 inhibitor in control cells.

Taken together, these results implicate GLI1-mediated Hedgehog signaling in the stem-like phenotype of OC induced by MGP.

The clinical relevance of MGP in OC

Our experimental data pointed to MGP as a driver of aggressiveness in OC. To clarify to what extent this applied to human disease, we first analyzed the expression of the protein in tissue samples from HGSOC or from the fimbriated end of healthy fallopian tubes, the main tissue of origin for this tumor type [41].

A

	Tumor take (day 100)	Tumor take (day 200)
OVCAR3-CTR	10/10	10/10
OVCAR3-MGP^{KO}	0/10	2/10

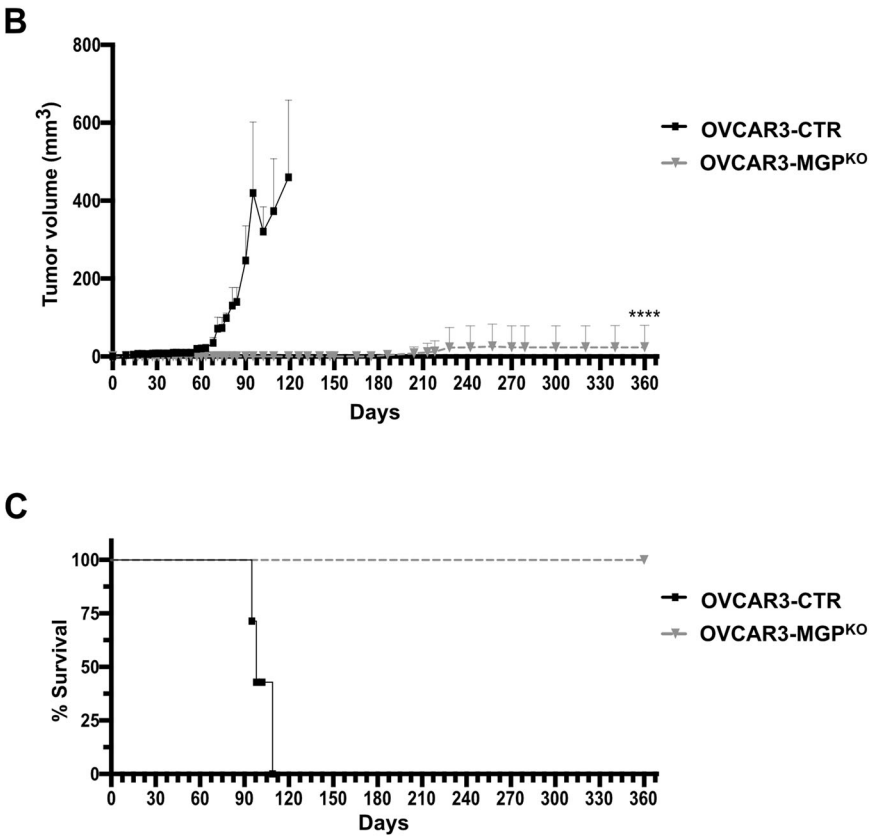

Fig. 5 MGP is required for tumor initiation and growth. A OVCAR3-CTR or OVCAR3-MGP^{KO} were injected subcutaneously into NOD-SCID mice at 5*10^6 cells/mouse ($n = 10$). Tumor take was assessed at day 100 and 200 and is expressed as mice with palpable tumors. **B** Tumor growth was monitored at different time points. Data are expressed as mean tumor volumes ± SEM. ****$p < 0.0001$. **C** Kaplan Meier survival analysis of mice injected with either OVCAR3-CTR or OVCAR3-MGP^{KO} cells. ****$p < 0.0001$.

Notably, MGP was detected at variable levels in all tumor samples. In contrast, no or low expression of MGP was found in healthy fimbriae (Fig. 9A). We then investigated the prognostic implications of MGP expression in OC by testing the correlation between MGP levels and the survival time in HGSOC patients from the TCGA cohort. Indeed, high MGP correlated significantly with shorter overall survival (HR 1.72; Fig. 9B, left). A similar trend was observed for disease-free survival, although statistical significance was not reached (HR 1.21; Fig. 9B, right). These data revealed that MGP is associated with poor prognosis in HGSOC patients. Of note, the *MGP* gene maps on 12p12.3, a hotspot for copy number alterations in OC (data available at https://www.cbioportal.org/), and, in fact, the gene was amplified in 8% of ovarian cancer in the TCGA cohort (Suppl. Fig. S4A). In agreement with the gene expression data reported in Fig. 9B, patients with *MGP* gene amplification had shorter overall survival than patients with no amplification (Suppl. Fig. S4B).

Finally, given that chemotherapy has been proposed to promote stem-like traits in OC cells [42–44], we investigated the expression levels of MGP in paired samples of OC collected from 19 patients before and after chemotherapy [45]. MGP was found to be consistently upregulated in post-treatment samples (Fig. 9C), suggesting that chemotherapy promotes an enrichment in MGP-expressing tumor cells.

DISCUSSION

While MGP alterations have been conclusively implicated in pathological calcification processes, their association with, and functional contribution to, neoplastic diseases remain controversial. For example, the downregulation of MGP has been proposed as a hallmark of colon carcinoma [46], but other investigators reported that colon cancer progression and worse prognosis are rather associated with higher MGP expression [14]. Contradictory results have also been published in glioblastoma, where both the upregulation and downregulation of MGP have been linked to tumor aggressiveness [47]. In general, whether MGP correlates with higher or lower aggressiveness depends on the tumor type or subtype. This is best exemplified by breast cancer, where MGP is downregulated in advanced HER2-positive tumors [48] while high levels are associated with the aggressive triple-negative subtype [13]. With regard to OC, Hough et al. reported that MGP is upregulated in this tumor type, yet with no indication on its prognostic value. We now confirmed and extended that

A

N. of cells transplanted	Tumor take (day 20)	Tumor take (day 40)
COV318-CTR 1*10^6	6/6	6/6
COV318-MGP 1*10^6	6/6	6/6
COV318-CTR 2*10^5	2/6	2/6
COV318-MGP 2*10^5	6/6	6/6
COV318-CTR 2*10^4	0/6	1/6
COV318-MGP 2*10^4	6/6	6/6
COV318-CTR 2*10^3	0/6	0/6
COV318-MGP 2*10^3	4/6	6/6
COV318-CTR 5*10^2	0/6	0/6
COV318-MGP 5*10^2	2/6	6/6
COV318-CTR 1*10^2	0/6	0/6
COV318-MGP 1*10^2	0/6	2/6
COV318-CTR 1*10^1	0/6	0/6
COV318-MGP 1*10^1	0/6	0/6

Group	Stem cell frequency
COV318-CTR	1/296618
COV318-MGP	1/277

B

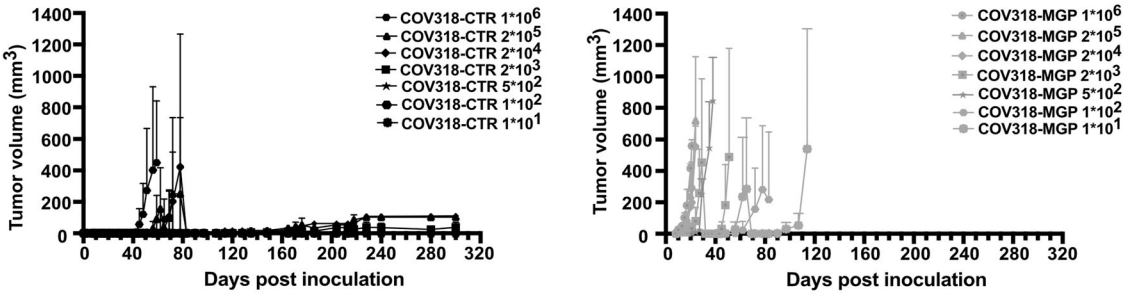

C

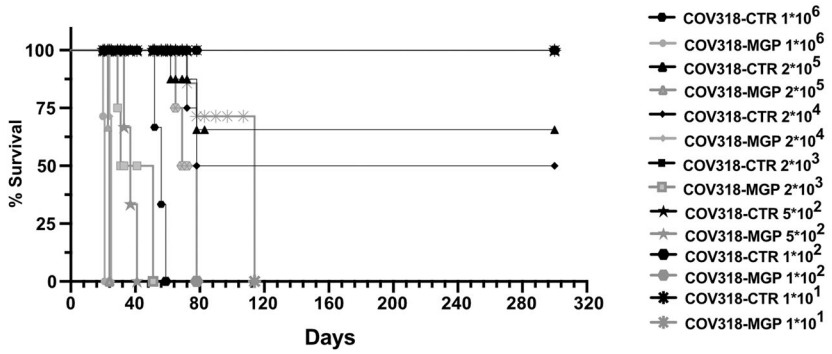

Fig. 6 MGP accelerates tumor initiation, increases cancer stem cell frequency and enhances tumor growth. A NOD-SCID mice were transplanted subcutaneously with decreasing numbers of either COV318-CTR or COV318-MGP cells and analyzed for tumor take at the indicated time points. Extreme limiting dilution assay (ELDA) was carried out to calculate the stem cell frequency ($p = 5.81*10^{-31}$). **B** The same mice were monitored over time and tumor volumes were measured. Data are expressed as means ± SEM. ****$p < 0.0001$ **C** Kaplan–Meier survival analysis of mice injected with decreasing numbers of either COV318-CTR or COV318-MGP cells. ****$p < 0.0001$, ***$p < 0.001$ for 10 cells.

observation by showing that the protein is detectable at variable level in OC but not in the tissue of origin, and its expression correlates with shorter survival in OC patients. The clinical value of MGP is further supported by our finding that MGP levels in OC are consistently increased upon treatment with chemotherapy, in agreement with the notion that the protein is associated with a highly malignant phenotype.

Our results strongly suggest that MGP upregulation is not a mere epiphenomenon of OC aggressiveness, but it rather reflects a functional contribution to tumor development. In particular, we report a novel role of MGP in the pathophysiology of OCSC and propose that such a role underlies the pro-tumorigenic function of MGP. By analogy to many other solid tumors, also in OC the subpopulation of CSC have been implicated in various aspects of disease progression. This paradigm seems particularly applicable to the clinical evolution of OC, which is characterized by high rate of metastatic spread, high frequency of relapse, and development of chemoresistance, all features commonly ascribed to CSC. Accordingly, various studies have identified neoplastic cells with stem-like traits that fuel OC spread and recurrence (reviewed in [3]). Nevertheless, the molecular and functional properties of OCSC have remained largely elusive due to different factors, one of the most prominent being the lack of clinically representative model systems. We have overcome this issue by relying on a series of

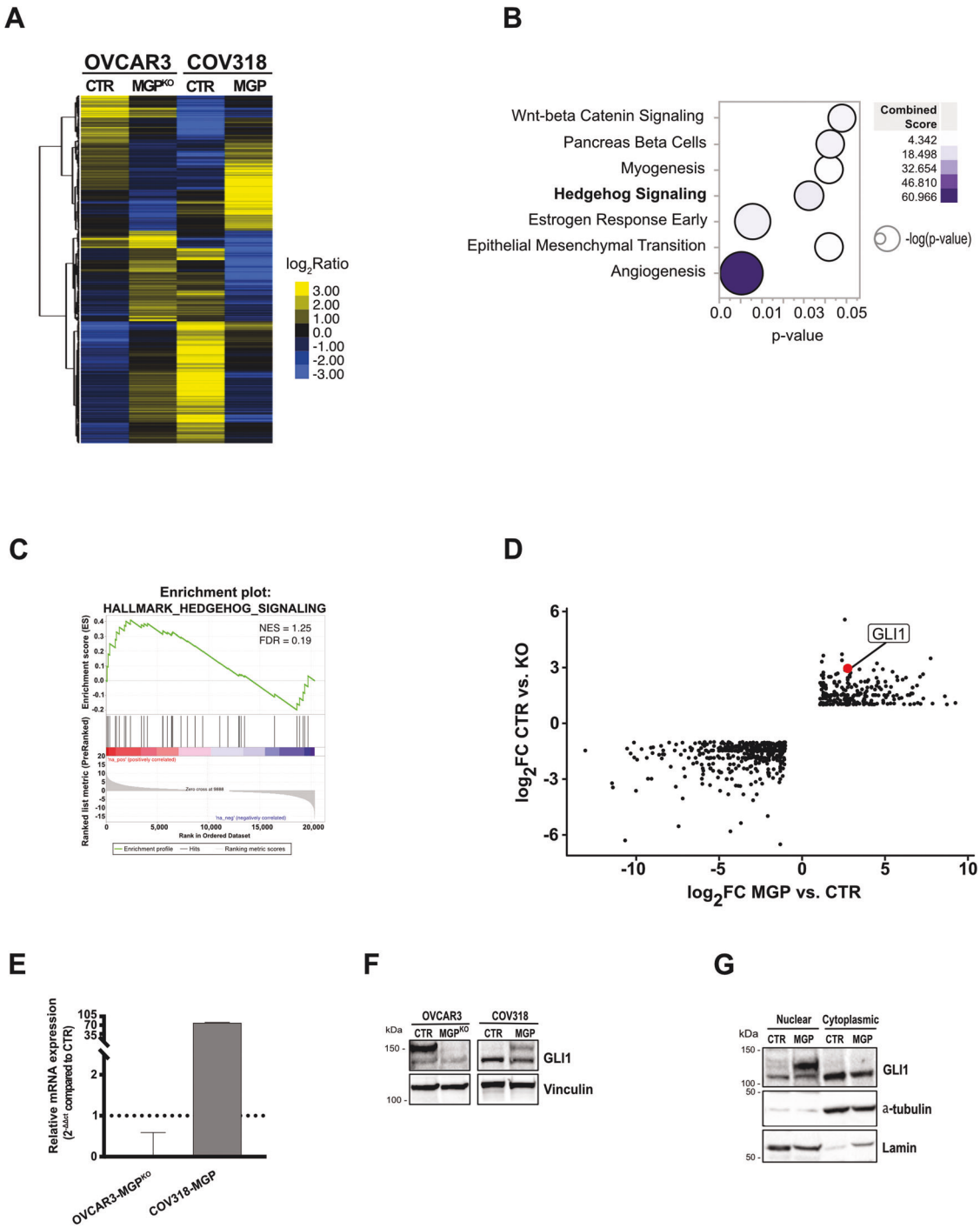

Fig. 7 MGP regulates gene expression in OCSC. A Hierarchical clustering analysis of MGP regulated genes in OVCAR3-CTR vs. OVCAR3-MGP^{KO} and COV318-CTR vs. COV318-MGP cells cultured as OCSC. The heatmap shows the expression of differentially regulated genes. The relative log_2FC ratio values of expression are indicated in the legend. **B** Bubble plot showing the EnrichR analysis using the HALLMARK GeneSets ($N = 38$) in COV318-MGP OCSC with opposite trend compared to OVCAR3-MGP^{KO}. Y-axes, GeneSets; X-axes, p-value of enrichment significance. Bubble size is proportional to inverse of Logarithmic (-Log) of *p*-value. Bubble colours refer to the combined score value, as per the legend. **C** Pre-ranked GSEA enrichment plots showing hallmark of cancer related to Hedgehog signaling pathway in COV318 cells cultured as OCSC. NES, normalized enrichment scores; FDR, significance of the enrichment (False Discovery Rate; 1000 random permutations); *p*, nominal p-value; 'na_pos' and 'na_neg' phenotypes correspond to enrichment in upregulated and downregulated genes, respectively. **D** Scatter plot showing the differentially expressed genes between OCSC overexpressing or knock-out for MGP. The x-axis represents the log2 fold change (log2FC) of OVCAR3-MGP^{KO} vs. OVCAR3-CTR cells. The y-axis represents the log2FC of COV318-CTR vs. COV318-MGP cells. The red dot indicates the position of GLI1. **E** qRT-PCR for GLI1 on OVCAR3-CTR vs. OVCAR3-MGP^{KO} and COV318-CTR vs. COV318-MGP cells. Data are expressed as the relative mRNA expression ($2^{-\Delta\Delta Ct}$) and normalized to the corresponding control cells (dashed line). Data refer to the means ± SD from a representative experiment performed in triplicate. **F** Immunoblot for GLI1 on MGP-manipulated OVCAR3 and COV318 cells. Vinculin was used as loading control. **G** Immunoblot for GLI1 on cytoplasmic and nuclear fractions from COV318-CTR vs. COV318-MGP cells. Alpha-tubulin and Lamin were used as loading controls for cytoplasmic and nuclear fractions, respectively.

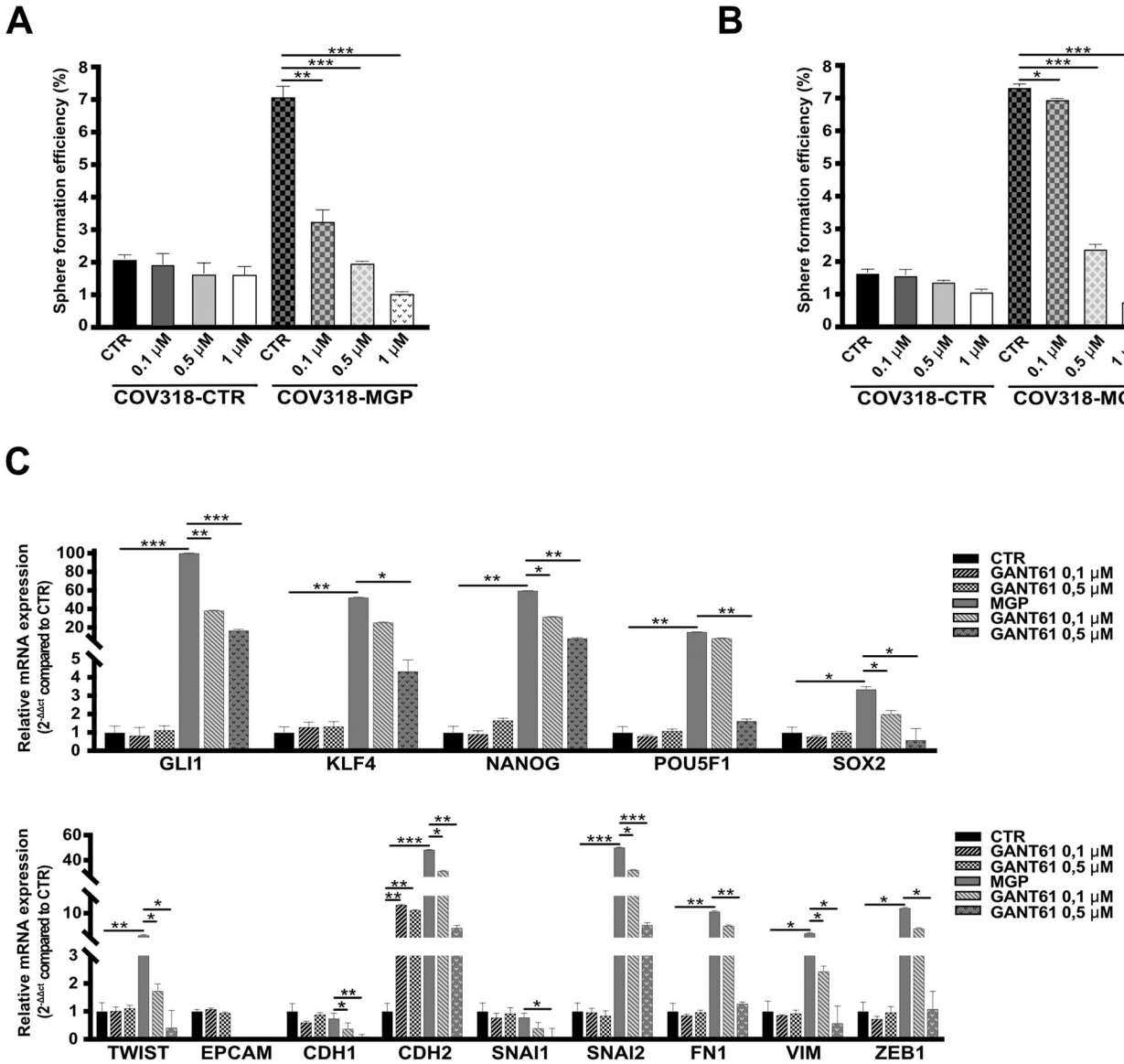

Fig. 8 MGP-induced stemness is mediated by Hedgehog signaling. COV318-CTR and COV318-MGP cells were treated with different concentrations of GANT61 (**A**) or cyclopamine (**B**) and subjected to sphere formation assay. For each analysis, results are shown as means ± SEM from two independent experiments. $^{**}p < 0.01$, $^{***}p < 0.001$. **C** qRT-PCR for stemness (top graph) and EMT-related genes (bottom graph) on COV318-CTR and COV318-MGP treated with 0.1 or 0.5 μM GANT61 for 48 h. Data are expressed as relative mRNA level ($2^{-\Delta\Delta Ct}$) and normalized to the COV318 control culture. Data refer to means ± SD from a representative experiment performed in triplicate.

patient-derived primary cultures, an approach that has recently revealed novel and unexpected players not only in OC per se but also in the OCSC subset [16, 17, 49, 50]. Along this line, primary cultures unveiled MGP as a hallmark of OCSC and provided the rationale for subsequent functional studies.

We could therefore show for the first time that MGP acts as a driver of cancer stemness, a function that entails the orchestration of a set of genes classically involved not only in dedifferentiation and multipotency but also in EMT, which is considered as an intrinsic feature and a causal player in the CSC phenotype [25]. Based on these findings, it is conceivable that the functional contribution of MGP to cancer stemness is not limited to OC. While, as outlined above, the role of MGP in cancer aggressiveness remains controversial and tumor type-dependent, we argue that in those cancers where MGP appears to exert a pro-tumorigenic function, such a function could entail the activation of the CSC subpopulation. Along the same line, future studies should test whether MGP expression represents a proxy for the "stemness" degree of a given tumor. This could have important therapeutic implications, especially in view of the emerging treatments that are being developed against CSC [51].

One of the most striking and unexpected findings in our study is the strong regulatory function exerted by MGP on the transcriptional activity of OC, with over 1600 genes showing opposite regulation upon MGP ablation vs. ectopic expression in bulk tumor cells and almost 1000 in OCSC. Such a massive regulation of the transcriptome, which is ascribed to MGP for the first time, most likely accounts for the pleiotropic function of the protein that we found in OC stemness. At the same time, the modulation of so many pathways that are known to play pivotal roles in tumor progression (e.g., hypoxia, angiogenesis, STAT5, etc.; Figs. 7B and S2E) raise the hypothesis that the role of MGP in OC extends well beyond stemness and orchestrates various aspects of cancer development. In agreement with the possible involvement of MGP in various cancer-related processes not necessarily related to OCSC, we observed a widespread distribution of the protein

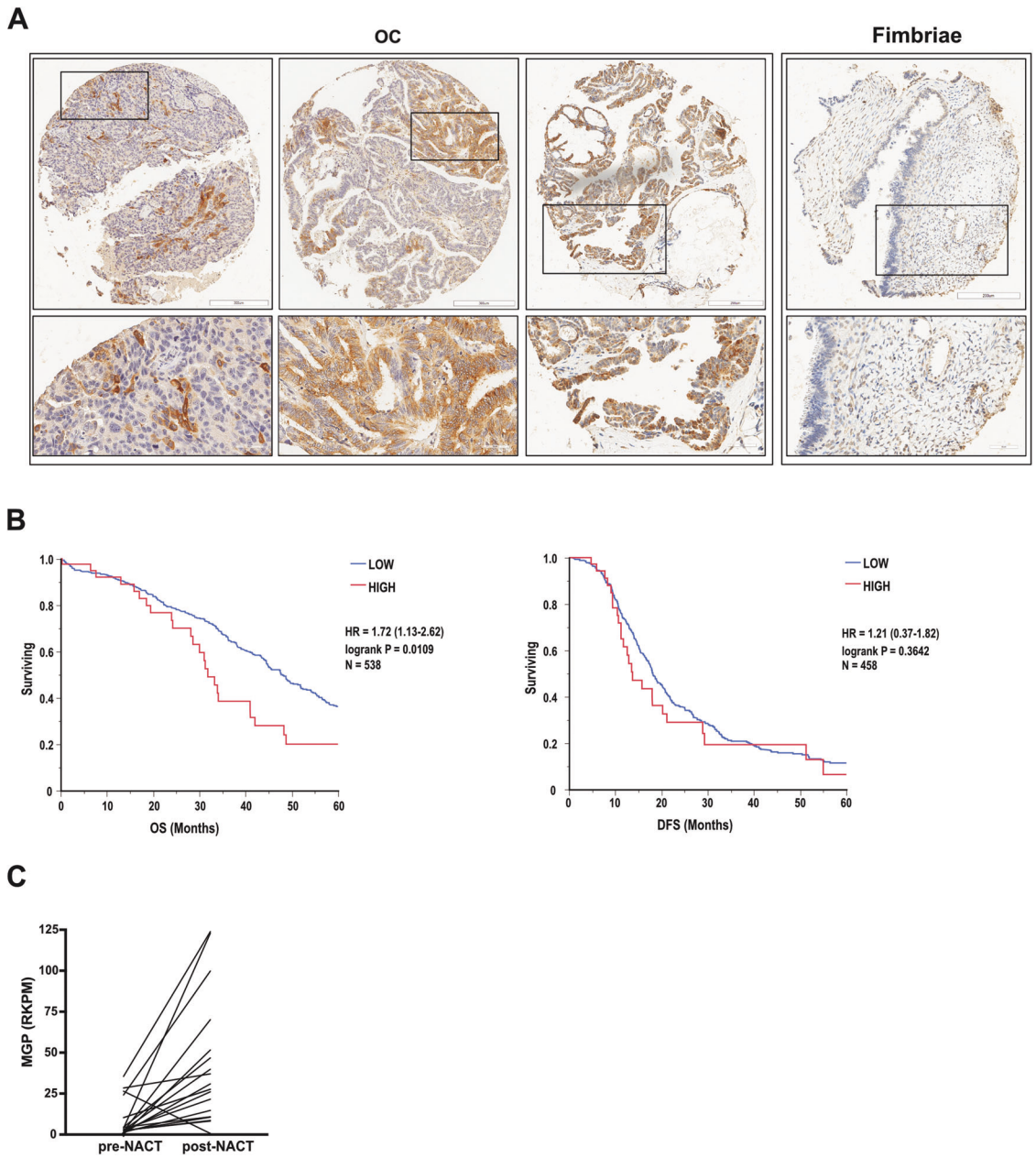

Fig. 9 Clinical relevance of MGP in human OC. A Sections of 3 representative OC samples and 1 fimbriae sample stained for MGP. Sections were counterstained with Hematoxylin. Lower panels show higher magnifications of the insets indicated in upper panels. The panels show representative images from a tissue microarray that included 120 tumors and 20 healthy fimbriae. Scale bars: 300 μm, upper panels; 50 μm, lower panels. **B** Survival analysis of TCGA-HGSOC patients stratified by MGP gene expression level (see methods). HIGH = high expression of MGP; LOW = low expression of MGP. Panels show overall survival (OS) on the left and disease-free survival (DFS) on the right. Log-rank p-values are displayed together with hazard ratio (HR, 95% Confidence Interval) and number of patients. **C** Expression of MGP in 19 patients before and after neoadjuvant chemotherapy (NACT). The data are obtained from the RNA-sequencing dataset published by Javellana et al [45], and are expressed as reads per kilobase million (RPKM). ***$p < 0.001$.

(*i.e.*, not restricted to small cancer cell subpopulations) in various OC specimens within our tissue microarrays (Fig. 9A).

Our study identified the Hedgehog pathway as a prominent effector of MGP-driven OC stemness, and implicated Hedgehog signaling in particular in self-renewal, and in the expression of multipotency and EMT-related genes. In this context, GLI1-mediated Hedgehog signaling has been implicated in various aspect of OC progression including cancer stemness. Aberrant Hedgehog signaling, indeed, is associated with reduced recurrence-free or overall survival in OC patients [52, 53]. The ectopic activation of the pathway in OC cells, for instance by GLI1 overexpression, promotes cell proliferation, cell mobility, and invasiveness [53]. GLI1 activity has also been reported to confer stem-like traits to OC cells, a function that is mediated by the multipotency-associated transcription factor NANOG [54]. Of note, NANOG is dramatically upregulated by MGP in our OCSC models thus raising the possibility of a MGP-GLI1-NANOG axis as a driver of OC stemness. Our finding that MGP-induced upregulation of NANOG is partially reverted by a GLI1 inhibitor (Fig. 8C) would support this hypothesis.

Our platform of fully patient-derived organotypic models revealed that the expression of MGP in OC cells is induced by contact with the peritoneal TME, that represents the most prominent site for metastasis and recurrence in this tumor type.

We also provided evidence that the TME enhances sphere formation in OC cells. These findings are consistent with the emerging view that a crosstalk with the peritoneal niche is essential for several stemness-associated features of OC, such as tumor initiation, metastasis, relapse, and therapy resistance [32]. Our data, besides providing further support to such a paradigm, suggest that regulating MGP expression is an integral part of the OCSC-orchestrating function of the peritoneal TME. It is intriguing that MGP, in turn, promotes the peritoneal adhesion and invasion of tumor cells, which points to this protein as a master regulator of the bi-directional crosstalk between the TME and OCSC. On a more general level, defining the TME-derived factors that induce and/or sustain OCSC activity in the context of metastasis and tumor recurrence will be instrumental to identify new actionable targets for OC eradication.

In summary, we have unveiled the novel and unexpected role of MGP as a master regulator of the pathophysiology of OCSC, as mirrored not only by its ability to promote self-renewal, the expression of stemness genes, and massive transcriptome changes, but also by a remarkable tumor-initiating potential. While providing new mechanistic insights into the pathogenic function of OCSC, our findings pave the way to further investigation on MGP and its downstream effectors in this context, which, in turn, may help designing innovative therapeutic strategies to defeat OCSC-driven tumor progression.

DATA AVAILABILITY

Raw mass spectrometry data have been deposited to the ProteomeXchange Consortium (http://proteomecentral.proteomexchange.org) [55] via the PRIDE partner repository [56] with the dataset identifier PXD037543.

REFERENCES

1. Marchetti C, De Felice F, Romito A, Iacobelli V, Sassu CM, Corrado G, et al. Chemotherapy resistance in epithelial ovarian cancer: Mechanisms and emerging treatments. Semin Cancer Biol. 2021;77:144–66.
2. Bray F, Ferlay J, Soerjomataram I, Siegel RL, Torre LA, Jemal A. Global cancer statistics 2018: GLOBOCAN estimates of incidence and mortality worldwide for 36 cancers in 185 countries. CA Cancer J Clin. 2018;68:394–424.
3. Lupia M, Cavallaro U. Ovarian cancer stem cells: Still an elusive entity? Mol Cancer; 2017. pp. 64.
4. Ayob AZ, Ramasamy TS. Cancer stem cells as key drivers of tumour progression. J Biomed Sci. 2018;25:20.
5. Cojoc M, Mäbert K, Muders MH, Dubrovska A. A role for cancer stem cells in therapy resistance: cellular and molecular mechanisms. Semin Cancer Biol. 2015;31:16–27.
6. Price PA, Urist MR, Otawara Y. Matrix Gla protein, a new gamma-carboxyglutamic acid-containing protein which is associated with the organic matrix of bone. Biochem Biophys Res Commun. 1983;117:765–71.
7. Luo G, Ducy P, McKee MD, Pinero GJ, Loyer E, Behringer RR, et al. Spontaneous calcification of arteries and cartilage in mice lacking matrix GLA protein. Nature. 1997;386:78–81.
8. Gheorghe SR, Crăciun AM. Matrix Gla protein in tumoral pathology. Clujul Med. 2016;89:319–21.
9. Sterzynska K, Klejewski A, Wojtowicz K, Swierczewska M, Andrzejewska M, Rusek D. et al. The Role of Matrix Gla Protein (MGP) Expression in Paclitaxel and Topotecan resistant ovarian cancer cell lines. Int J Mol Sci. 2018;19:2901.
10. Levedakou EN, Strohmeyer TG, Effert PJ, Liu ET. Expression of the matrix Gla protein in urogenital malignancies. Int J Cancer. 1992;52:534–7.
11. Yoshimura K, Takeuchi K, Nagasaki K, Ogishima S, Tanaka H, Iwase T, et al. Prognostic value of matrix Gla protein in breast cancer. Mol Med Rep. 2009;2:549–53.
12. Zandueta C, Ormazábal C, Perurena N, Martínez-Canarias S, Zalacaín M, Julián MS, et al. Matrix-Gla protein promotes osteosarcoma lung metastasis and associates with poor prognosis. J Pathol. 2016;239:438–49.
13. Gong C, Zou J, Zhang M, Zhang J, Xu S, Zhu S, et al. Upregulation of MGP by HOXC8 promotes the proliferation, migration, and EMT processes of triple-negative breast cancer. Mol Carcinog. 2019;58:1863–75.
14. Li X, Wei R, Wang M, Ma L, Zhang Z, Chen L, et al. MGP promotes colon cancer proliferation by activating the NF-κB pathway through upregulation of the calcium signaling pathway. Mol Ther Oncolytics. 2020;17:371–83.
15. Wang M, Chen L, Chen Y, Wei R, Guo Q, Zhu S, et al. Intracellular matrix Gla protein promotes tumor progression by activating JAK2/STAT5 signaling in gastric cancer. Mol Oncol. 2020;14:1045–58.
16. Francavilla C, Lupia M, Tsafou K, Villa A, Kowalczyk K, Rakownikow Jersie-Christensen R, et al. Phosphoproteomics of primary cells reveals Druggable kinase signatures in ovarian cancer. Cell Rep. 2017;18:3242–56.
17. Lupia M, Angiolini F, Bertalot G, Freddi S, Sachsenmeier KF, Chisci E, et al. CD73 regulates stemness and Epithelial-Mesenchymal transition in ovarian cancer-initiating cells. Stem Cell Rep. 2018;10:1412–25.
18. Bache N, Geyer PE, Bekker-Jensen DB, Hoerning O, Falkenby L, Treit PV, et al. A novel LC system embeds analytes in pre-formed gradients for rapid, ultra-robust proteomics. Mol Cell Proteom. 2018;17:2284–96.
19. Bekker-Jensen DB, Martínez-Val A, Steigerwald S, Rüther P, Fort KL, Arrey TN, et al. A compact Quadrupole-Orbitrap Mass Spectrometer with FAIMS interface improves proteome coverage in short LC gradients. Mol Cell Proteom. 2020;19:716–29.
20. Bruderer R, Bernhardt OM, Gandhi T, Miladinović SM, Cheng LY, Messner S, et al. Extending the limits of quantitative proteome profiling with data-independent acquisition and application to acetaminophen-treated three-dimensional liver microtissues. Mol Cell Proteom. 2015;14:1400–10.
21. Labun K, Montague TG, Krause M, Torres Cleuren YN, Tjeldnes H, Valen E. CHOPCHOP v3: expanding the CRISPR web toolbox beyond genome editing. Nucleic Acids Res. 2019;47:W171–w174.
22. Liberzon A, Birger C, Thorvaldsdóttir H, Ghandi M, Mesirov JP, Tamayo P. The Molecular Signatures Database (MSigDB) hallmark gene set collection. Cell Syst. 2015;1:417–25.
23. Hänzelmann S, Castelo R, Guinney J. GSVA: gene set variation analysis for microarray and RNA-seq data. BMC Bioinforma. 2013;14:7.
24. Liberzon A, Subramanian A, Pinchback R, Thorvaldsdóttir H, Tamayo P, Mesirov JP. Molecular signatures database (MSigDB) 3.0. Bioinformatics. 2011;27:1739–40.
25. Lambert AW, Weinberg RA. Linking EMT programmes to normal and neoplastic epithelial stem cells. Nat Rev Cancer. 2021;21:325–38.
26. Barnes BM, Nelson L, Tighe A, Burghel GJ, Lin IH, Desai S, et al. Distinct transcriptional programs stratify ovarian cancer cell lines into the five major histological subtypes. Genome Med. 2021;13:140.
27. Domcke S, Sinha R, Levine DA, Sander C, Schultz N. Evaluating cell lines as tumour models by comparison of genomic profiles. Nat Commun. 2013;4:2126.
28. Radajewska A, Przybyszewski O, Emhemmed F, Muller CD, Barg E, Moreira H. Three dimensional in vitro culture systems in anticancer drug discovery targeted on cancer stem cells. Am J Cancer Res. 2021;11:4931–46.
29. Gotoh N. Control of stemness by fibroblast growth factor signaling in stem cells and cancer stem cells. Curr Stem Cell Res Ther. 2009;4:9–15.
30. Otte J, Dizdar L, Behrens B, Goering W, Knoefel WT, Wruck W, et al. FGF signalling in the self-renewal of colon cancer organoids. Sci Rep. 2019;9:17365.
31. Davidowitz RA, Iwanicki MP, Brugge JS. In vitro mesothelial clearance assay that models the early steps of ovarian cancer metastasis. J Vis Exp. 2012;60:3888.
32. Motohara T, Yoshida GJ, Katabuchi H. The hallmarks of ovarian cancer stem cells and niches: Exploring their harmonious interplay in therapy resistance. Semin cancer Biol. 2021;77:182–93.
33. Kenny HA, Krausz T, Yamada SD, Lengyel E. Use of a novel 3D culture model to elucidate the role of mesothelial cells, fibroblasts and extra-cellular matrices on adhesion and invasion of ovarian cancer cells to the omentum. Int J Cancer. 2007;121:1463–72.
34. Hu Y, Smyth GK. ELDA: Extreme limiting dilution analysis for comparing depleted and enriched populations in stem cell and other assays. J Immunol Meth. 2009;347:70–8.
35. Ray A, Meng E, Reed E, Shevde LA, Rocconi RP. Hedgehog signaling pathway regulates the growth of ovarian cancer spheroid forming cells. Int J Oncol. 2011;39:797–804.
36. Pak E, Segal RA. Hedgehog signal transduction: key players, oncogenic drivers, and cancer therapy. Dev Cell. 2016;38:333–44.
37. Pietrobono S, Gagliardi S, Stecca B. Non-canonical Hedgehog signaling pathway in cancer: Activation of GLI transcription factors beyond smoothened. Front Genet. 2019;10:556.
38. Lauth M, Bergström A, Shimokawa T, Toftgård R. Inhibition of GLI-mediated transcription and tumor cell growth by small-molecule antagonists. Proc Natl Acad Sci USA. 2007;104:8455–60.
39. Chen JK, Taipale J, Cooper MK, Beachy PA. Inhibition of Hedgehog signaling by direct binding of cyclopamine to Smoothened. Genes Dev. 2002;16:2743–8.
40. Axelson M, Liu K, Jiang X, He K, Wang J, Zhao H, et al. U.S. Food and Drug Administration approval: vismodegib for recurrent, locally advanced, or metastatic basal cell carcinoma. Clin Cancer Res. 2013;19:2289–93.
41. Klotz DM, Wimberger P. Cells of origin of ovarian cancer: ovarian surface epithelium or fallopian tube? Arch Gynecol Obstet. 2017;296:1055–62.
42. Abubaker K, Latifi A, Luwor R, Nazaretian S, Zhu H, Quinn MA, et al. Short-term single treatment of chemotherapy results in the enrichment of ovarian cancer

stem cell-like cells leading to an increased tumor burden. Mol Cancer. 2013;12:24.
43. Rizzo S, Hersey JM, Mellor P, Dai W, Santos-Silva A, Liber D, et al. Ovarian cancer stem cell-like side populations are enriched following chemotherapy and overexpress EZH2. Mol Cancer Ther. 2011;10:325–35.
44. Zhu H, Gu X, Xia L, Zhou Y, Bouamar H, Yang J, et al. A Novel TGFβ trap blocks chemotherapeutics-induced TGFβ1 signaling and enhances their anticancer activity in gynecologic cancers. Clin Cancer Res. 2018;24:2780–93.
45. Javellana M, Eckert MA, Heide J, Zawieracz K, Weigert M, Ashley S, et al. Neoadjuvant chemotherapy induces genomic and transcriptomic changes in ovarian cancer. Cancer Res. 2022;82:169–76.
46. Fan C, Sheu D, Fan H, Hsu K, Allen Chang C, Chan E. Down-regulation of matrix Gla protein messenger RNA in human colorectal adenocarcinomas. Cancer Lett. 2001;165:63–9.
47. Mertsch S, Schurgers LJ, Weber K, Paulus W, Senner V. Matrix gla protein (MGP): an overexpressed and migration-promoting mesenchymal component in glioblastoma. BMC Cancer. 2009;9:302.
48. Tuo YL, Ye YF. MGP is downregulated due to promoter methylation in chemoresistant ER+ breast cancer and high MGP expression predicts better survival outcomes. Eur Rev Med Pharm Sci. 2017;21:3871–8.
49. Giordano M, Decio A, Battistini C, Baronio M, Bianchi F, Villa A, et al. L1CAM promotes ovarian cancer stemness and tumor initiation via FGFR1/SRC/STAT3 signaling. J Exp Clin Cancer Res. 2021;40:319.
50. Lupia M, Melocchi V, Bizzaro F, Riso PL, Dama E, Baronio M, et al. Integrated molecular profiling of patient-derived ovarian cancer models identifies clinically relevant signatures and tumor vulnerabilities. Int J Cancer. 2022;151:240–54.
51. Bisht S, Nigam M, Kunjwal SS, Sergey P, Mishra AP, Sharifi-Rad J. Cancer stem cells: from an insight into the basics to recent advances and therapeutic targeting. Stem Cells Int. 2022;2022:9653244.
52. Chen X, Horiuchi A, Kikuchi N, Osada R, Yoshida J, Shiozawa T, et al. Hedgehog signal pathway is activated in ovarian carcinomas, correlating with cell proliferation: it's inhibition leads to growth suppression and apoptosis. Cancer Sci. 2007;98:68–76.
53. Liao X, Siu MK, Au CW, Wong ES, Chan HY, Ip PP, et al. Aberrant activation of hedgehog signaling pathway in ovarian cancers: effect on prognosis, cell invasion and differentiation. Carcinogenesis. 2009;30:131–40.
54. Zhao H, Li N, Pang Y, Zhao J, Wu X. Gli affects the stemness and prognosis of epithelial ovarian cancer via homeobox protein NANOG. Mol Med Rep. 2021;23:128.
55. Deutsch EW, Csordas A, Sun Z, Jarnuczak A, Perez-Riverol Y, Ternent T. et al. The ProteomeXchange consortium in 2017: supporting the cultural change in proteomics public data deposition. Nucleic Acids Res. 2017;45:D1100–D1106.
56. Perez-Riverol Y, Bai J, Bandla C, Garcıa-Seisdedos D, Hewapathirana S, Kamatchinathan S. et al. The PRIDE database resources in 2022: a hub for mass spectrometry-based proteomics evidences. Nucleic Acids Res. 2022;50:D543–D552.

ACKNOWLEDGEMENTS

We are grateful to all patients who donated their samples for this work. We thank A. Gatto for technical assistance with primary cultures, G. Jodice, S. Freddi and S. Pece for the immunohistochemical analyses, E. Lengyel and H. Kenny for kindly providing omental primary cells. P. Nicoli for assistance with the mouse experiments. We thank the staff of Division of Gynecology and of Biobank at IEO for providing clinical specimens. Fabrizio Bianchi wishes to dedicate this work to the memory of Lucia, an extraordinary girl who experienced cancer as an opportunity to entrust her and all her loved ones to the love of the Father.

AUTHOR CONTRIBUTIONS

VN, JVO, FB, and UC contributed to the concept and design of the study. VN, CB, GF, ML, and CS performed experiments. NC provided clinical specimens. VM, GF, GB, and FB contributed to the analysis and interpretation of results. VN, FB, and UC wrote the manuscript. All authors reviewed and approved the manuscript.

FUNDING

This work was supported by grants from Associazione Italiana Ricerca sul Cancro [IG-14622 and IG-21320 to U.C., MFAG-17568, and IG-22827 to F.B.], the Italian Ministry of Health [RF-2016-02362551 to U.C., GR-2016-02363975 and CLEARLY to F.B.], the Ovarian Cancer Research Alliance [648516 to U.C.] Fondazione IEO-Monzino [Grant to U.C.], Roche per la Ricerca [Grant to M.L.]. V.N. and M.L. were supported by fellowships from Fondazione IEO-Monzino and Fondazione Umberto Veronesi. The work performed at CPR was funded by the European Proteomics Infrastructure Consortium providing access, EPIC-XS (Grant number 1162431015). The study funders had no role in the design of the study, collection, analysis, and interpretation of the data, writing of the manuscript, and decision to submit the manuscript for publication.

MATERIALS AVAILABILITY

All materials area available from the authors upon reasonable request. Affymetrix and RNAseq data were deposited in Gene Expression Omnibus database (http://www.ncbi.nlm.nih.gov/geo/) with the accession numbers GSE216627 and GSE216487, respectively.

COMPETING INTERESTS

The authors declare no competing interests.

ETHICAL APPROVAL

Informed consent was obtained from the patients enrolled in the study. This study was performed in accordance with the Declaration of Helsinki and was approved by the European Institute of Oncology Ethics Committee (protocol no. R789-IEO). Animal studies were performed following protocols approved by the fully authorized animal facility of the European Institute of Oncology and by the Italian Ministry of Health (as required by the Italian Law) (protocol no. 325/2016) and in accordance with EU directive 2010/63.

ADDITIONAL INFORMATION

Supplementary information The online version contains supplementary material available at https://doi.org/10.1038/s41419-023-05760-w.

Correspondence and requests for materials should be addressed to U. Cavallaro.

Reprints and permission information is available at http://www.nature.com/reprints

Publisher's note Springer Nature remains neutral with regard to jurisdictional claims in published maps and institutional affiliations.